

**Electron Identification Performance and First Measurement of
 $W \rightarrow e + \nu$ Process with the ATLAS Detector**

by

Ryuichi (Rick) Ueno

A thesis submitted to the
Faculty of Graduate and Postdoctoral Affairs
in partial fulfillment of the requirements
for the degree of
Master of Science

Ottawa-Carleton Institute for Physics
Department of Physics
Carleton University
Ottawa, Ontario, Canada
September, 2010

©copyright
Ryuichi (Rick) Ueno, 2010



Library and Archives
Canada

Published Heritage
Branch

395 Wellington Street
Ottawa ON K1A 0N4
Canada

Bibliothèque et
Archives Canada

Direction du
Patrimoine de l'édition

395, rue Wellington
Ottawa ON K1A 0N4
Canada

Your file *Votre référence*
ISBN: 978-0-494-71600-7
Our file *Notre référence*
ISBN: 978-0-494-71600-7

NOTICE:

The author has granted a non-exclusive license allowing Library and Archives Canada to reproduce, publish, archive, preserve, conserve, communicate to the public by telecommunication or on the Internet, loan, distribute and sell theses worldwide, for commercial or non-commercial purposes, in microform, paper, electronic and/or any other formats.

The author retains copyright ownership and moral rights in this thesis. Neither the thesis nor substantial extracts from it may be printed or otherwise reproduced without the author's permission.

In compliance with the Canadian Privacy Act some supporting forms may have been removed from this thesis.

While these forms may be included in the document page count, their removal does not represent any loss of content from the thesis.

AVIS:

L'auteur a accordé une licence non exclusive permettant à la Bibliothèque et Archives Canada de reproduire, publier, archiver, sauvegarder, conserver, transmettre au public par télécommunication ou par l'Internet, prêter, distribuer et vendre des thèses partout dans le monde, à des fins commerciales ou autres, sur support microforme, papier, électronique et/ou autres formats.

L'auteur conserve la propriété du droit d'auteur et des droits moraux qui protègent cette thèse. Ni la thèse ni des extraits substantiels de celle-ci ne doivent être imprimés ou autrement reproduits sans son autorisation.

Conformément à la loi canadienne sur la protection de la vie privée, quelques formulaires secondaires ont été enlevés de cette thèse.

Bien que ces formulaires aient inclus dans la pagination, il n'y aura aucun contenu manquant.


Canada

Abstract

The identification of electrons is important for the ATLAS experiment because electrons are present in many interactions of interest produced at the Large Hadron Collider. A deep knowledge of the detector, the electron identification algorithms, and the calibration techniques are crucial in order to accomplish this task. This thesis work presents a Monte Carlo study using electrons from the $W \rightarrow e + \nu$ process to evaluate the performance of the ATLAS electromagnetic calorimeter. A significant number of electrons was produced in the early ATLAS collision runs at centre-of-mass energies of 900 GeV and 7 TeV between November 2009 and April 2010, and their properties are presented. Finally, a first measurement of $W \rightarrow e + \nu$ process with the ATLAS experiment was successfully accomplished with the first $\mathcal{L} = 1.0 \text{ nb}^{-1}$ of data at the 7 TeV collision energy, and the properties of the W candidates are also detailed.

Acknowledgements

First and foremost, I would like to thank my supervisor, Dr. Manuella Vincter, for her patience and great support and guidance with this work.

I would also like to thank the members of the Ecal team and the Egamma working group in the ATLAS collaboration with whom I had privilege working on various tasks. Without their help I would have been lost and could not have produced the results presented here.

Needless to say, I could not have achieved this accomplishment without my colleagues at Carleton. Not only did they assist me and contribute constructive feedbacks, but also provided a bright and friendly environment both on and off campus.

I would not have been writing this without my parents. Their interest in my studies have fueled me to work harder at it.

Last but not least, I would like to thank my wonderful fiancée Kelly. Thank you for your support and encouragement even when I was across the ocean.

Contents

Abstract	ii
Acknowledgments	iii
List of Tables	vi
List of Figures	vii
1 Introduction and Motivation	1
1.1 General Introduction	1
1.2 The LHC and ATLAS	3
1.2.1 The LHC	3
1.2.2 The ATLAS Experiment	5
1.3 Motivation for the Thesis Topic	5
1.4 Synopsis of the Thesis Topic	7
2 ATLAS Detector	8
2.1 The Inner Detector System	10
2.2 The Calorimeter System	12
2.3 The Muon System	15
2.4 The Trigger System	16
2.5 The ATLAS Offline Software	17
3 Electronic Calibration of the ATLAS EM Calorimeter	18
3.1 EM Shower Development	19

3.2	ATLAS EM Calorimeter	23
3.3	Energy Reconstruction in the EM Calorimeter	27
3.4	Calibration of the EM Calorimeter	31
3.5	Stability Study of the EM Calorimeter	33
4	Calorimeter Energy Response Study	37
4.1	Methodology	38
4.1.1	The Sample Datasets	38
4.1.2	The Selection Requirements	40
4.1.3	Energy Response Distribution as a Study Parameter	40
4.1.4	The Fitting	41
4.2	Comparison of Athena 14.2.25 Version and Athena 15.3.0 Version	43
4.3	Material Distortion	48
4.4	Study of Bremsstrahlung Effects	52
4.5	Summary	55
5	Electron Performance and W Boson Searches with Early Data	57
5.1	Electron Candidates in Early ATLAS Data	59
5.1.1	Kinematics Properties of Electron Candidates	59
5.1.2	Electron Identification Requirements	63
5.2	W Boson Searches with Early Data	67
5.2.1	Monte Carlo Samples and Expected Backgrounds	68
5.2.2	W Identification	69
5.2.3	W Properties in 7 TeV Data	73
5.3	Summary	77
6	Conclusion	79
A	Personal Contributions to the ATLAS Collaboration	82
	References	83

List of Tables

1.1	List of fundamental particles as defined by the Standard Model	2
2.1	Granularity of the ATLAS calorimeter	13
3.1	Threshold values of calibration parameters used for validation	33
5.1	Cross-section of physics processes considered for analysis	68
5.2	Number of $W \rightarrow e + \nu$ candidates after selection	73
5.3	Expected number of signal and background events	77

List of Figures

1.1	Injection chain at the LHC	4
2.1	The overall layout of the ATLAS detector	9
2.2	The overall layout of the ATLAS ID system	10
2.3	The overall layout of the ATLAS calorimeter system	12
2.4	The overall layout of the ATLAS muon system	15
3.1	A schematic drawing of an example EM shower	20
3.2	An example longitudinal energy loss profile	22
3.3	The overall and detailed view of the LAr calorimeter system	24
3.4	Schematic drawing of an EMB module	25
3.5	Schematic drawing of an FEB module	27
3.6	Digitization of an ionization signal	28
3.7	Example signal pulse for calibration and physics	30
3.8	Stability plots for combined EMB and EMEC	35
4.1	An example of energy response distribution	42
4.2	Comparison of energy response for Athena versions 14 and 15	43
4.3	Detail of the impact of calculation error in Athena version 14	45
4.4	Comparison of energy response width for Athena versions 14 and 15	45
4.5	Comparison of energy response width to the material distribution in front of the EM calorimeter	46
4.6	The modulation for calorimeter energy response	47
4.7	The setup of the MC simulation with distorted material	49
4.8	The impact of extra materials on energy response	50

4.9	The impact of material distribution on the calorimeter response	51
4.10	Map of distorted material distribution for the ID in the MC simulation	51
4.11	Diagram for bremsstrahlung of $W \rightarrow e + \nu$ decay	52
4.12	Comparison of energy response with and without internal bremsstrahlung	53
4.13	Energy response distribution by bremsstrahlung type	54
4.14	Fraction of events in the tail of the energy response distribution	55
5.1	Kinematics properties of electron candidates	61
5.2	Evaluation of efficiency, rejection and purity of electron identification algorithm	64
5.3	Comparison of shower width in η in real data	65
5.4	Comparison of number of pixel hits in real data	66
5.5	Comparison of TRT hits ratio in real data	66
5.6	The spectrum of M_T from MC simulation	72
5.7	Kinematics properties of events after preselection	74
5.8	2D plot of E_T^{miss} vs M_T	75
5.9	Plot of M_T before and after E_T^{miss} requirement	76
5.10	E_T and p_T of the Lepton- E_T^{miss} system after the final selection	76

Chapter 1

Introduction and Motivation

1.1 General Introduction

Since the early twentieth century, the interplay of theoretical developments and precision measurements, made available by technological advances, has led to the formulation of the Standard Model (SM) of particle physics. The SM postulates the existence of “elementary particles” which can be grouped into either fermions or bosons, depending on the intrinsic spin of the particle, as depicted in Figure 1.1. This model also describes particle interactions via the exchange of force carriers. For example, the Coulomb force is described by the electromagnetic interaction mediated by a photon γ , radiation decay by the weak interaction mediated by a W^\pm or a Z boson, and quarks are bound by the strong interaction mediated by a gluon g . The SM also postulates a mechanism for which particles acquire mass and explains why certain particles are massless (such as photons and gluons) while others are massive. This mechanism, called the Higgs mechanism [1],

Quarks (spin = 1/2)				Leptons (spin = 1/2)				Gauge Bosons (spin = 1)			
Flavour		Mass (GeV/c ²)	Charge	Flavour		Mass (GeV/c ²)	Charge	Name	Mass (GeV/c ²)	Charge	
u	up	0.003	2/3	ν_e	electron neutrino	<1x10 ⁻⁸	0	γ	photon	0	0
d	down	0.005	-1/3	e	electron	0.000511	-1	W⁺	W ⁺ boson	80.4	+1
c	charm	1.27	2/3	ν_μ	muon neutrino	<0.0002	0	W⁻	W ⁻ boson	80.4	-1
s	strange	0.101	-1/3	μ	muon	0.106	-1	Z⁰	Z boson	91.19	0
t	top	172	2/3	ν_τ	tau neutrino	<0.002	0	g	gluon	0	0
b	bottom	4.3	-1/3	τ	tau	1.777	-1				

Table 1.1: List of fundamental particles as defined by the Standard Model. The left two columns list the fermions (spin = 1/2) while the right column lists the bosons (spin = 1), also known as the force-carriers.

introduces an additional massive boson called the Higgs boson. However, it has not yet been discovered, and thus there is a significant emphasis on the search for this missing piece of the model.

The SM has been consistent with most experimental observations up to date [2, 3]; however, some recent measurements has required it to adapt and evolve. For example, neutrino experiments, such as Sudbury Neutrino Observatory [4] and Super-Kamiokande [5], have measured neutrino flavour mixing. This is only possible if neutrinos have mass. However, they are treated as massless particles in the SM. Similar discoveries have lead to modifications that allow the SM to accommodate these discrepancies, and also fueled interest for models that extend the SM, often referred to as Beyond the Standard Model (BSM). However, most of these BSM interactions occur only at high energy scale and so are challenging to observe.

The Tevatron at Fermilab [6, 7] has been at the energy frontier in particle accelerators for the past 20 years. It accelerates protons p and anti-protons \bar{p} to a centre-of-mass

energy¹ of 1.9 TeV and collides them to initiate interactions with one another. At this energy scale, the cross-sections for some interesting physics processes (Higgs boson production, for example) are significantly lower than other less-interesting processes such as jet production. At higher collision energy, the cross-sections for some of these physics signals of interest increase in comparison to other processes. Therefore, a particle accelerator must be capable of producing higher collision energy and luminosity (number of particle interactions per unit area per time) in order to probe new physics.

1.2 The LHC and ATLAS

1.2.1 The LHC

The Large Hadron Collider (LHC) is a high-energy particle accelerator located at CERN (Conseil Européenne pour la Recherche Nucléaire), near Geneva Switzerland [8]. It is designed to accelerate two proton beams, each proton beam made up of 2,808 “bunches” consisting of approximately 10^{11} protons, around its 27 km long beam pipe buried 100 m underground. The accelerated beams will have unprecedented energy of up to 14 TeV centre-of-mass energy and luminosity of $10^{34} \text{ cm}^{-2}\text{s}^{-1}$.

In order to achieve such high collision energy, it uses four stages of acceleration chains before reaching the main LHC ring (See Figure 1.1). The initial proton acceleration is achieved using a linear accelerator (LINAC2) up to an energy of 50 MeV. The accelerated protons then are fed into the Proton Synchrotron Booster (PSB) which further accelerates

¹Natural units ($c = \hbar = 1$) are used throughout this work, therefore energy, momentum and mass all have units of eV.

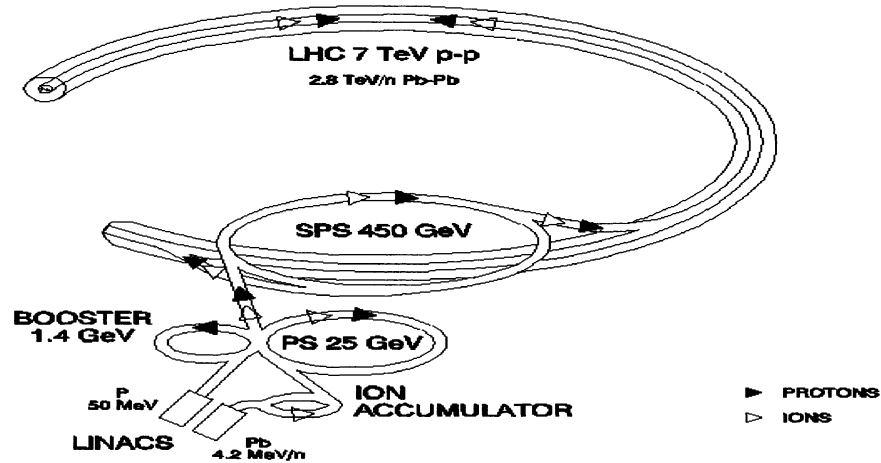


Figure 1.1: Injection chain at the LHC. It is designed to accelerate both protons (to 7 TeV) and lead ions (to 2.8 TeV). Figure from [8].

the protons to 1.4 GeV. The protons from the PSB are subsequently injected into the Proton Synchrotron (PS) and accelerated to 25 GeV, the Super Proton Synchrotron (SPS) to 450 GeV and finally into the main LHC ring which accelerates to the final beam energy of 7 TeV. At the design luminosity of $10^{34} \text{ cm}^{-2}\text{s}^{-1}$, the proton beams collide at an interval of 25 ns. Aside from protons, the LHC is also designed to accelerate heavy ions; in particular fully stripped lead ions ($^{208}\text{Pb}^{82+}$) at 2.76 TeV/nucleon.

The LHC houses four main experiments: ATLAS [9], ALICE [10], CMS [11], and LHCb [12]. Of the four experiments, ATLAS and CMS are general-purpose detectors. ALICE is optimized for heavy ion collisions to study quark gluon plasma. LHCb is dedicated to the study of a charge-conjugation/parity (CP) violation and rare decay events, particularly of the “bottom” quark. This thesis work involves the ATLAS experiment

exclusively.

1.2.2 The ATLAS Experiment

The ATLAS detector is the biggest at the LHC and has features that most modern particle detectors have, namely charged-particle tracking, calorimetry and muon detection. However, ATLAS uses some new design features to accommodate the high collision energy, luminosity, and event rate of the LHC without degradation of its performance. Refer to Chapter 2 for a more in-depth discussion of the ATLAS detector.

There is a vast physics programme at ATLAS involving both SM and BSM processes. SM studies include precision measurements of cross-sections and masses of W and Z bosons (carriers of the weak interactions), and of the top quark (first discovered at the Tevatron in 1995 [6]). These measurements contribute to the determination of the SM parameters such as Weinberg (or weak mixing) angle θ_W . In addition, the Higgs boson search is one of the main foci of the experiment, because it is one of the missing pieces in the SM that is expected to be observable at the LHC energy scale. BSM studies include searches for supersymmetry (SUSY), extra-dimension signatures, and more exotic Higgs models. In particular, SUSY is an attractive model, since some of the supersymmetric partners of the SM particles are viable candidates for dark matter.

1.3 Motivation for the Thesis Topic

Although the main focus of the ATLAS experiment is the new physics, analyses of previously well-studied particles are as important. Identification of electrons is vital be-

cause they are present in many of the interactions produced in ATLAS. For example, the SM Higgs boson can decay to Z bosons, which subsequently decay to electrons ($H \rightarrow Z + Z \rightarrow e + e + e + e$).

The reconstruction and identification of electrons are not trivial tasks, due to the interactions of these particles with the ATLAS detector and to the complexity of this detector. It requires detailed knowledge of the detector, behaviour of the electron interaction with the detector material, as well as proper calibration of the detector.

The performance of the detector can be studied using computer-simulated information (referred to as Monte Carlo or MC events) and real collision data. Electrons from $p - p$ collisions are primarily produced from the decay of other particles. One of the most clean and probable sources is the leptonic decay of the W boson, whose production cross-section is about 10^4 times larger than that of Higgs boson production at the LHC energy scale [13]. This produces an electron (or positron, depending on the charge of the W boson²) and a neutrino. That is:

$$W^- \rightarrow e^- + \bar{\nu}, \quad (1.1)$$

$$W^+ \rightarrow e^+ + \nu. \quad (1.2)$$

The electrons from early ATLAS running are useful for understanding the detector. Conversely, they can be used to make precision measurements of the W boson properties once the detector is well-understood. These precision measurements have an impact on other areas of the physics programmes at ATLAS. For instance, the mass of the W boson and of the top quarks are the largest sources of uncertainty in indirect Higgs boson mass

²For this thesis, a charge conjugation is assumed. So the term “electron” generally refers to both electrons and positrons.

determination [14].

This thesis work deals with both identification of electrons and evaluation of detector performance using electrons with Monte Carlo simulations, calibration techniques, as well as real collision data from early data taking. In addition, identification of W bosons through leptonic decays and study of their properties in early running of the LHC are also presented.

1.4 Synopsis of the Thesis Topic

The rest of this thesis is organized in individual chapters. Chapter 2 gives an overview of the ATLAS detector as well as specific components of the detector that are relevant to this study. Chapter 3 details how the particle energies are measured inside the electromagnetic calorimeter, and the calibration techniques used in ATLAS. Chapter 4 details the study of external impacts on energy response in the ATLAS electromagnetic calorimeter using Monte Carlo simulation. Chapter 5 presents the identification of electrons and W bosons from early collision data. Finally, Chapter 6 summarizes this work. Additionally, Appendix A lists my personal contributions to the ATLAS collaboration for the duration of this work.

Chapter 2

ATLAS Detector

ATLAS (**A Toroidal LHC ApparatuS**) [9] is one of the two general-purpose detectors at the LHC (**L**arge **H**adron **C**ollider) [8], the other being CMS (**C**ompact **M**uon **S**olenoid) [11]. ATLAS is designed as a typical multi-purpose particle detector for use in a high-energy proton-proton collider, with hopes to validate or refute current theories and to discover new physics. Due to the unprecedented high energy (14 TeV centre-of-mass energy) and luminosity ($10^{34} \text{ cm}^{-2}\text{s}^{-1}$) of the LHC design, the ATLAS detector must in turn accommodate the interaction rate and radiation dose from the collisions at the LHC.

The ATLAS detector is shown in Figure 2.1. The detector has dimension of 25 m in height and 44 m in length, and weighs approximately 7,000 tonnes. The ATLAS detector is positioned such that the beam direction defines the z -axis, the positive x -axis points from the centre of the detector (interaction point) towards the centre of the LHC ring, and the positive y -axis points from the interaction point upwards. The positive and

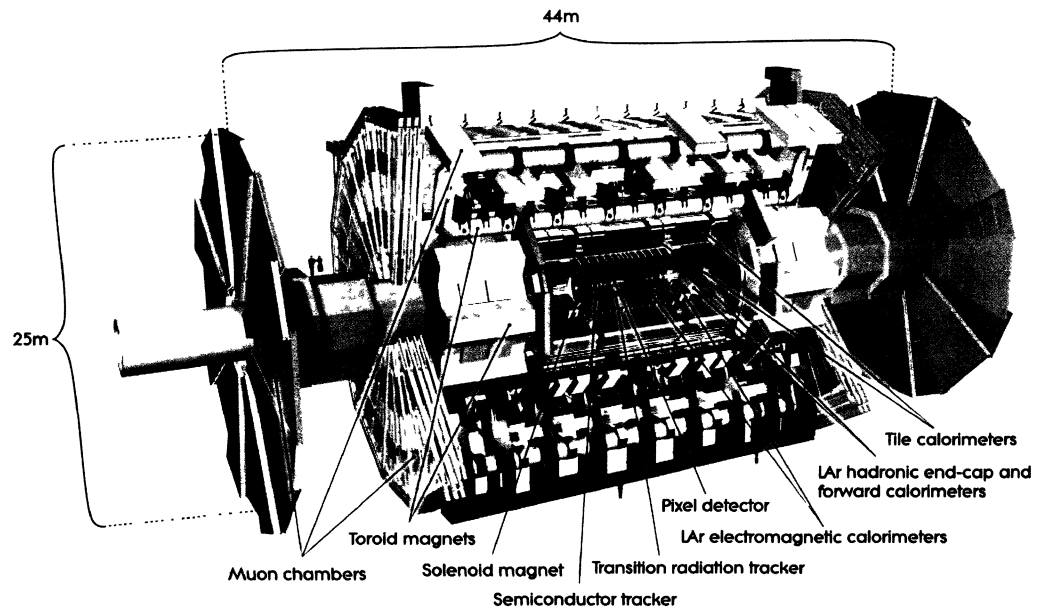


Figure 2.1: The cut-away view of the ATLAS detector showing the major components. Figure from [9]

negative z -axes are defined as side-A and side-C, respectively. The azimuthal angle ϕ is measured around the beam axis, and the polar angle θ is measured from the beam axis. Instead of polar angle, pseudorapidity is more commonly used in collider physics, since the particle production is approximately constant in this space, and it is defined as $\eta = -\ln \tan(\theta/2)$ [2].

The ATLAS detector is mainly comprised of four components: the inner detector system, the calorimetry system, the muon system, and the trigger system. Aside from the main detector components, the offline software also plays an important role. Each of

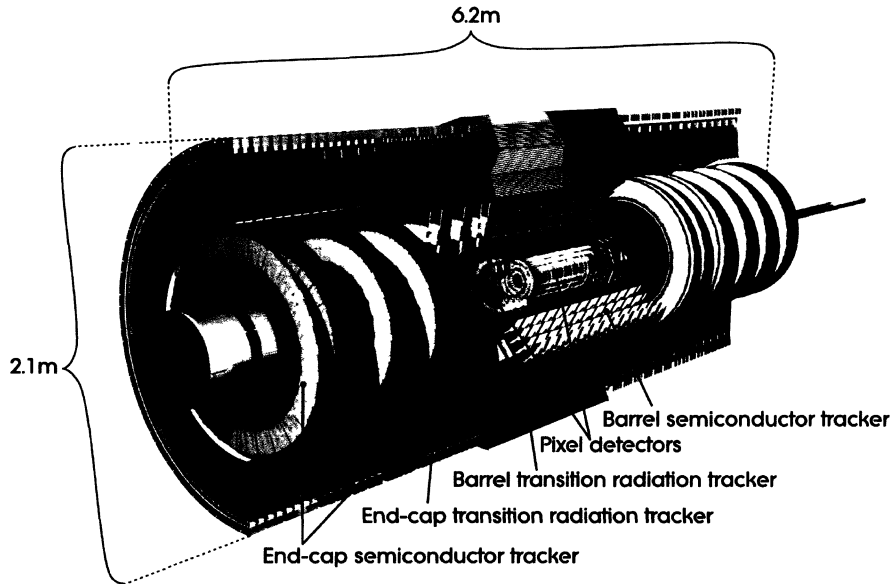


Figure 2.2: The overall layout of the ATLAS inner detector system. Figure from [9]

these components is described further in detail in the following sections.

2.1 The Inner Detector System

The inner detector system (ID) [9] is the structure closest to the interaction point in ATLAS. Its primary role is the measurement of the momentum of charged particles as well as vertexing for decaying particles. It covers the region $|\eta| < 2.5$, and it is under a 2 T magnetic field from the central solenoid. The ID is comprised of three components: pixel detector, semiconductor tracker (SCT), and transition radiation tracker (TRT). Figure 2.2 shows the details of the layout of the ID.

The pixel detector uses a novel technology in order to withstand the high radiation flux. It is a series of silicon detector “pixels” measuring $50\ \mu\text{m} \times 400\ \mu\text{m}$. There are three concentric pixel layers near the beam pipe, where the closest layer (also called the “b-layer”) is located $\sim 50\ \text{mm}$ from the beam pipe. In the end-cap regions ($|\eta| > 2.0$), three layers are arranged perpendicular to the beam direction. Due to its high granularity, the pixel detector has 80.4 million readout channels.

The SCT is a more traditional silicon micro-strip detector. The SCT provides accurate information over a larger area than the pixel detector while minimizing the overall cost. Four SCT layers are arranged in concentric layers outside the pixel detector. In the end-cap regions ($|\eta| > 1.5$), nine layers are placed perpendicular to the beam direction similar to the pixel layers. The total number of readout channels in the SCT is approximately 6.3 million.

The TRT is a straw-tube detector that uses a xenon gas mixture, and it surrounds both the pixel detector and the SCT in the region $|\eta| < 2.0$. The polyimide “straw” drift tubes are arranged parallel to the beam pipe in the central region, while in the end-cap regions ($|\eta| > 1.0$) they are arranged radially. The TRT detects the transition-radiation photons from the radiator within the structure, and it provides useful information for electron detection that complements the calorimeter information. The TRT has approximately 351,000 readout channels.

The combined ID has momentum resolution of $\sigma_{p_T}/p_T = 0.05\%/\sqrt{\text{GeV}} \cdot p_T \oplus 1\%$, where p_T is measured in GeV [9], and it is an essential component of the electron identification algorithm, which will be described in Section 5.1.2.

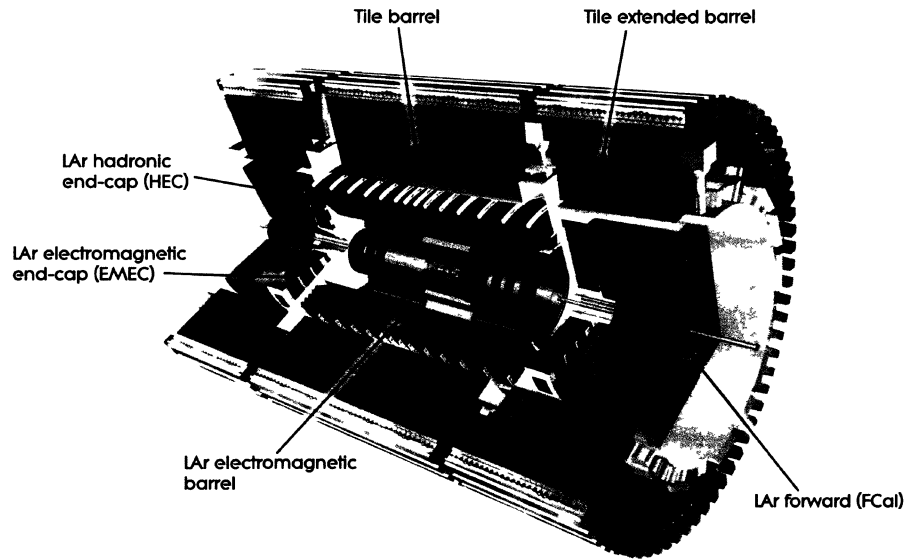


Figure 2.3: The overall layout of the ATLAS calorimeter system. Figure from [9].

2.2 The Calorimeter System

Figure 2.3 shows the layout of the ATLAS calorimeter system [9]. It surrounds the inner detector system and is responsible for the measurement of the energy of particles and jets. It is also capable of deducing the energy escaped from a collision event (known as missing transverse energy). To accomplish this, the ATLAS calorimeter has high $\Delta\eta \times \Delta\phi$ granularity and large pseudorapidity coverage ($|\eta| < 4.9$). Table 2.1 details the granularity at specific parts of the calorimeter. The ATLAS calorimeter consists of two types: electromagnetic (EM) and hadronic.

The ATLAS EM calorimeter is specifically optimized for the detection of electromag-

	Barrel		Endcap	
Presampler	0.025 × 0.1	$ \eta < 1.52$	0.025 × 0.1	1.5 < $ \eta $ < 1.8
EM S1	0.025/8 × 0.1	$ \eta < 1.40$	0.050 × 0.1	1.375 < $ \eta $ < 1.425
	0.025 × 0.025	1.40 < $ \eta $ < 1.475	0.025 × 0.1	1.425 < $ \eta $ < 1.5
			0.025/8 × 0.1	1.5 < $ \eta $ < 1.8
			0.025/6 × 0.1	1.8 < $ \eta $ < 2.0
			0.025/4 × 0.1	2.0 < $ \eta $ < 2.4
			0.025 × 0.1	2.4 < $ \eta $ < 2.5
EM S2	0.025 × 0.025	$ \eta < 1.40$	0.050 × 0.025	1.375 < $ \eta $ < 1.425
	0.075 × 0.025	1.40 < $ \eta $ < 1.475	0.025 × 0.025	1.425 < $ \eta $ < 2.5
			0.1 × 0.1	2.5 < $ \eta $ < 3.2
EM S3	0.050 × 0.025	$ \eta < 1.35$	0.050 × 0.025	1.5 < $ \eta $ < 2.5
HEC			0.1 × 0.1	1.5 < $ \eta $ < 2.5
			0.2 × 0.2	2.5 < $ \eta $ < 3.2
FCal1 $\Delta x \times \Delta y$ (cm)			3.0 × 2.6	3.15 < $ \eta $ < 4.30
			~ four times finer	3.10 < $ \eta $ < 3.15, 4.30 < $ \eta $ < 4.83
FCal2 $\Delta x \times \Delta y$ (cm)			3.3 × 4.2	3.24 < $ \eta $ < 4.50
			~ four times finer	3.20 < $ \eta $ < 3.24, 4.50 < $ \eta $ < 4.81
FCal3 $\Delta x \times \Delta y$ (cm)			5.4 × 4.7	3.32 < $ \eta $ < 4.60
			~ four times finer	3.29 < $ \eta $ < 3.32, 4.60 < $ \eta $ < 4.75
TileCal S1,S2	0.1 × 0.1	$ \eta < 1.0$	0.1 × 0.1	0.8 < $ \eta $ < 1.7
TileCal S3	0.2 × 0.1	$ \eta < 1.0$	0.2 × 0.1	0.8 < $ \eta $ < 1.7

Table 2.1 Granularity ($\Delta\eta \times \Delta\phi$ unless otherwise specified) of the ATLAS calorimeter. The EM calorimeter is the primary object of this study, it is described more in detail in Section 3.2. It is a sampling calorimeter with alternating layers of lead absorbers and liquid argon (LAr) ionizing material, and it covers the entire ϕ space of ATLAS detector. The EM calorimeter is largely divided into two separate parts. The barrel component covers the range $|\eta| < 1.475$ while the end-cap component covers the range $1.375 < |\eta| < 3.2$. The EM calorimeter has three sampling layers with different granularity (See Table 2.1).

The ATLAS hadronic calorimeter detects hadronic showers and jets and it surrounds the EM calorimeter (See Figure 2.3). It consists of two types: the tile calorimeter and

the LAr hadronic end-cap calorimeter (HEC). The tile calorimeter is divided into a barrel ($|\eta| < 1.0$) and an extended barrel ($0.8 < |\eta| < 1.7$) regions. The tile calorimeter has steel absorbers and scintillating tiles, and the signals are read out via wavelength-shifting optical fibres. For the HEC, there are two wheels covering $1.5 < |\eta| < 3.2$. It uses copper layers as absorbers and LAr as the active ionizing material. The hadronic tile calorimeter has three layers while the HEC has four layers.

In the forward region ($3.1 < |\eta| < 4.9$), there exist the forward calorimeters (FCal) consisting of one EM layer and two hadronic layers. The EM and hadronic FCal use copper and tungsten as absorbers respectively, and both use LAr as active ionizing material.

The energy resolution of a calorimeter is expressed as [2]:

$$\frac{\sigma_E}{E} = \frac{a}{\sqrt{E}} \oplus b \oplus \frac{c}{E} \quad (2.1)$$

where \oplus represents addition in quadrature and E is in GeV. The stochastic term a represents the statistical fluctuations, the constant term b is related to detector imperfections and calibration errors, and the noise term c is from the electronics used in the calorimeter. The stochastic and the noise terms have units of $\sqrt{\text{GeV}}$ and GeV respectively. The energy resolution of the EM calorimeter is $\sigma_E/E = 10\%/\sqrt{E} \oplus 0.7\%$ [9]. The hadronic calorimeter has energy resolution of $\sigma_E/E = 50\%/\sqrt{E} \oplus 3\%$ [9]. Finally, the energy resolution of the FCal is $\sigma_E/E = 100\%/\sqrt{E} \oplus 10\%$ [9]. The energy resolution of the combined calorimeter system was determined from a test beam study conducted in 1996, where a test module at $|\eta| = 0.25$ was subjected to pion beams with energy ranging from 10 to 300 GeV. The energy resolution was found to be $\sigma_E/E = 52\%/\sqrt{E} \oplus 3\% \oplus 1.6/E$,

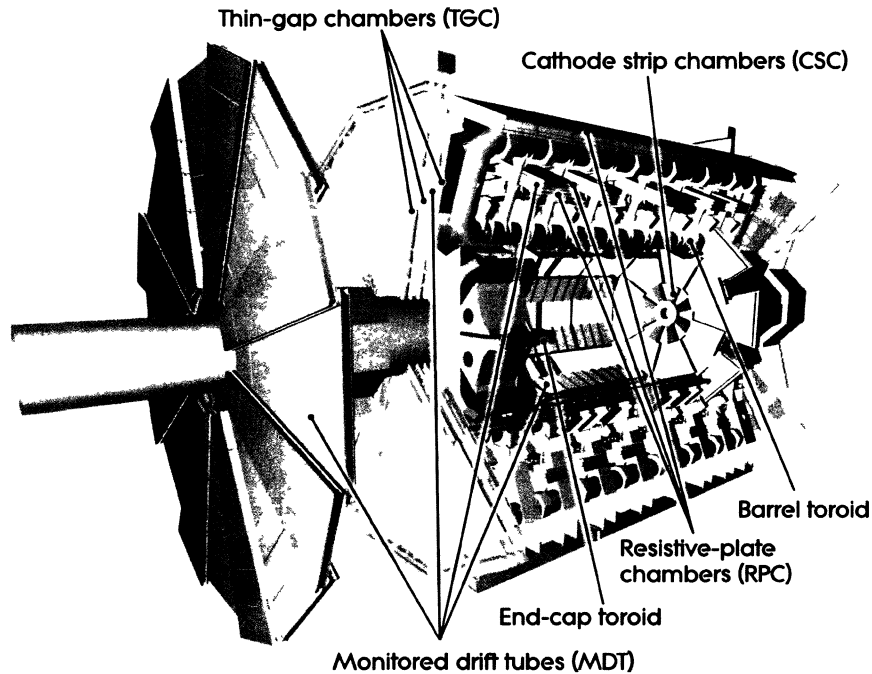


Figure 2.4: The overall layout of the ATLAS muon system. Figure from [9]

where E is in GeV [9].

2.3 The Muon System

The ATLAS muon system is designed to detect muons and measure their momentum. It is located outside of the calorimeter system, and the layout of the muon system is depicted in Figure 2.4. The magnet system consists of large barrel toroid magnets in the range $|\eta| < 1.4$ and end-cap toroids on either side of the detector that bend the muons in the range $1.6 < |\eta| < 2.7$.

The precise muon detection is provided by Monitored Drift Tubes (MDT) in most of the pseudorapidity range, and Cathode Strip Chambers (CSC) in the end-cap regions ($2.0 < |\eta| < 2.7$). These are paired with trigger chambers [Resistive Plate Chamber (RPC) in the barrel regions and Thin Gap Chamber (TGC) in the end-cap region] that are used as threshold detectors in the range $|\eta| < 2.4$. There are 1,150 MDT chambers and 606 RPC in the barrel region, while 32 CSC and 3,588 TGC are present in the end-cap region.

The muon spectrometer is designed to have the transverse momentum resolution of $\sigma_{p_T}/p_T < 3\%$ for low p_T ($p_T \sim 100$ GeV) and $\sigma_{p_T}/p_T = 10\%$ for high p_T ($p_T > 1$ TeV) [9].

2.4 The Trigger System

The LHC's proton-proton interaction rate at the design luminosity of 10^{34} cm⁻²s⁻¹ is approximately 1 GHz, while the event data recording is limited to 200 Hz. The sophisticated ATLAS trigger is designed to achieve this reduction while maintaining the maximum efficiency needed for new physics. In order to achieve this, a three-stage trigger system is used: Level 1 (L1), Level 2 (L2) and Event Filter (EF).

The hardware-based L1 trigger takes information from the calorimeter and muon spectrometer at coarser granularity to reduce the rate to 75 kHz in less than 2.5 μ s. When an event passes these trigger criteria, L1 also defines the region of interest (ROI) that contains the η and ϕ location of the event, and feeds into the L2 triggering system.

L2 and EF together are referred to as High-Level Trigger (HLT) and it is a software-

based trigger system. L2 trigger takes the information from L1 and refines the events in the ROI using all available detector information (i.e. including the ID which is not used for L1 and using the full available granularity). The L2 is able to reduce the rate to 3.5 kHz with a latency of about 40 ms. The EF trigger then performs the final stage of the event selection. The EF selections will reduce the rate to 200 Hz with a latency of approximately four seconds, and output events are classified as electrons, muons, jets, photons, E_T^{miss}/τ -leptons and B -physics.

2.5 The ATLAS Offline Software

Once the events from the collisions pass all of the trigger criteria, data are stored for the offline analysis. The ATLAS offline software framework is called Athena [14], and its main purpose is calibration, event reconstruction, physics analysis, and production of Monte Carlo (MC) simulated events. Because all of these analyses are intertwined and related to each other, this makes the framework complex. Consequently, Athena is subject to regular and frequent updates with a turn-around time of 4 to 6 months for each release.

Each release includes pieces of algorithms that are improved from the older version or in some cases newly created in order to build accurate simulation models and to conduct proper physics analyses. However, there is a need to quantify the validity of these improvements. Within this study period, the Athena software package had a major version upgrade from version 14 to 15. Section 4.2 details results of some of this validation.

Chapter 3

Electronic Calibration of the ATLAS EM Calorimeter

The ATLAS liquid-argon (LAr) calorimeter, introduced in Section 2.2, is designed to measure the energy of particles with great precision (of order 0.1% for the mean response of the EM calorimeter). It is also a large and complex device that depends on various parameters to properly reconstruct the energy of an incoming particle. Because of the complexity of its design, it is sensitive to various environmental conditions. Any deviation from the normal operational state may result in mis-measurements of particle energies.

As with most sensitive measuring instruments, regular calibration is an important step. Calibration measurements characterize how the calorimeter behaves under certain conditions, and thus infer the change in parameters that affect proper energy calculation. Calibration measurements will also keep track of misbehaving or problematic channels which may lead to incorrect energy reconstruction.

There is a dedicated group within the ATLAS collaboration whose main responsibility is to take calibration measurements and to validate the results (Electronic calibration, or “Ecal” team). The Ecal team consists of members who are assigned to validate a specific LAr subdetector, and experts who consult with the members to make decisions on any potential modifications. During the summer 2009 period, I was a member of the Ecal team and was involved in the validation of calibration constants in the EMB (EM Barrel) subdetector as well as the study of stability of these constants in time. See Section 3.4 for a further description of the validation process.

Proper calibration of the LAr calorimeter requires sufficient knowledge on how particles interact with the detector, how the detector collects the signal deposited by the particle, and how the software reconstructs the energy from the information from the readout. These are described in the subsequent sections. For the rest of the chapter, exclusively the electromagnetic (EM) part of the LAr calorimeter (hence interactions of EM particles) will be discussed.

3.1 EM Shower Development

Calorimetry in particle physics refers to the measurement of particle energy. Particle energy is a very important piece of information that is used for particle identification (including mass measurements) as well as quantification of various Standard Model parameters. It also gives information about overall interactions such as missing energy, which is an integral part of many Beyond the Standard Model physics searches.

Calorimeters determine energies by measuring the energy lost by the incoming particle

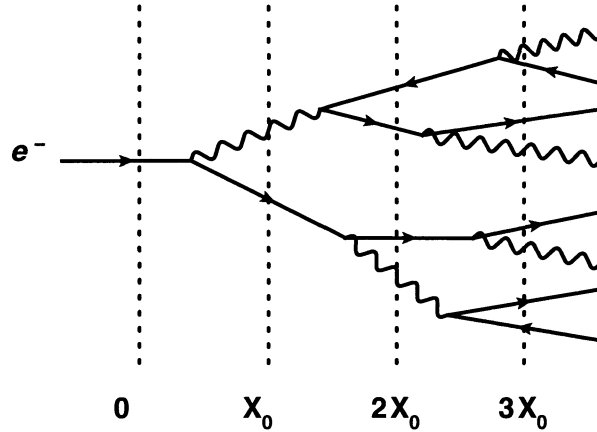


Figure 3.1: An example of an EM shower. Straight lines indicate electron paths, while wavy lines indicate photons. Right-bound arrows represent electrons, while left-bound arrows represent positrons. The vertical lines indicate the depth in radiation lengths.

due to interactions with the calorimeter materials. In particular, an electromagnetic calorimeter makes energy measurements of showers involving electrons, positrons and photons. For the specific details of the ATLAS EM calorimeter, see Section 3.2.

When high-energy (greater than a few tens of MeV) electrons, positrons or photons interact with the calorimeter material, two interaction processes dominate [2, 15]. One is pair production, where a photon near a strong nuclear or atomic electric field converts into an electron and a positron ($\gamma \rightarrow e^- + e^+$). The other dominating interaction is a process known as bremsstrahlung, where an incident electron or positron interacts with the coulomb field of the material, radiating a photon ($e^\pm \rightarrow e^\pm + \gamma$). The subsequent interactions will develop an EM shower (see Figure 3.1).

An EM shower profile is commonly noted in terms of radiation lengths X_0 [15]. One

radiation length is the average distance which an electron travels before interacting and losing $(1 - 1/e)$ of its initial energy due to bremsstrahlung [2]. For photons, one radiation length is $7/9$ of the mean free path for pair production. A radiation length can be approximated for a given material by [2]:

$$X_0 = \frac{1}{\rho} \frac{716.4 \text{ g} \cdot \text{cm}^{-2} A}{Z(Z+1) \ln(287/\sqrt{Z})} [\text{cm}], \quad (3.1)$$

where ρ is the density of the material in $\text{g} \cdot \text{cm}^{-3}$, and A and Z are the mass number and atomic number of the material, respectively. For lead, the absorber material used in the ATLAS EM calorimeter, the radiation length is $X_0 = 0.57$ cm.

The longitudinal profile of an EM shower describes the depth to which a particle penetrates the calorimeter before all of its energy is lost. The mean longitudinal energy loss of the EM shower with initial energy E_0 is described by the equation [2]:

$$\frac{dE}{dt} = E_0 b \frac{(bt)^{a-1} e^{-bt}}{\Gamma(a)}, \quad (3.2)$$

where a and b are material-specific parameters, $t = x/X_0$ is the shower depth, and Γ is the gamma function. The scale parameter b is also dependent on the initial energy deposition E , but it can be approximated for heavy materials ($Z > Z_{Fe}$) as $b \approx 0.5$. The value of a can then be calculated using the relation for shower depth that gives maximum dE/dt , which is expressed in units of radiation lengths as:

$$t_{max} = \frac{a-1}{b} = \ln \frac{E}{E_c} + C_i, \quad (3.3)$$

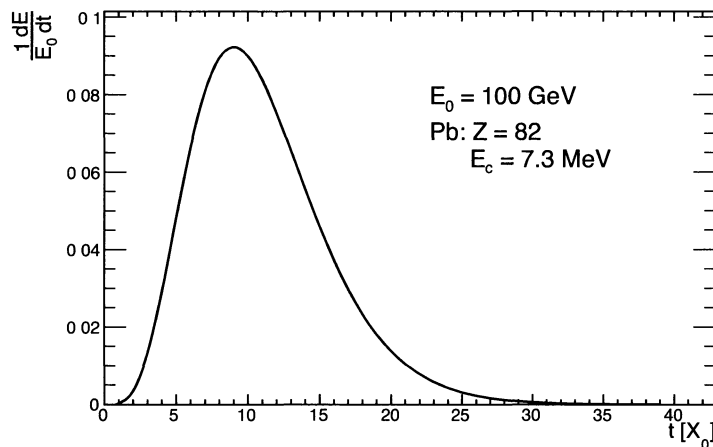


Figure 3.2: Longitudinal energy loss profile for 100 GeV electron in lead material. The peak corresponds to $t_{max} = 9.0X_0$.

where $C_i = -0.5$ for electrons and E_c is the critical energy. The critical energy is the energy at which an electron's energy loss via ionization (dominating interaction at low energy) and bremsstrahlung (dominating interaction at high energy) are approximately equal [2]. E_c for electrons inside solids and liquids is given by [2]:

$$E_c = \frac{610 \text{ MeV}}{Z + 1.24}. \quad (3.4)$$

For lead, $E_c \approx 7.3 \text{ MeV}$. Consequently, this gives $t_{max} \approx 9.0X_0$ for 100 GeV incident electrons, and therefore $a \approx 5.5$. Figure 3.2 shows the longitudinal energy loss profile for 100 GeV electron in lead material. The thickness of $24 X_0$ is required to contain 99 % of the longitudinal incident energy.

The transverse profile of an EM shower refers to the width of the shower, and it scales

with the Molière radius, given by [2]:

$$R_M = X_0 \frac{21.2 \text{MeV}}{E_c} [\text{cm}]. \quad (3.5)$$

Approximately 90% of the EM shower is contained in a cylinder of 1 Molière radius, and 99% shower containment in $3.5R_M$. For lead, the Molière radius is $R_M = 1.65$ cm. Therefore, the transverse profile of an EM shower is independent of the incident energy. At higher energies, the particles cascade at smaller angles, but travel further longitudinally, resulting in a longer shower shape.

3.2 ATLAS EM Calorimeter

In order to measure the energy deposited by the cascading EM showers described above, ATLAS has a dedicated sampling EM calorimeter based on liquid-argon (LAr) technology. It is located between the inner detector system and the hadronic tile calorimeter system. The LAr EM system is comprised of the EM Barrel (EMB), and the EM End-Cap (EMEC). For their respective locations, refer to Figure 2.3. The EMB covers the region $|\eta| < 1.475$ with a 4 mm gap at $\eta = 0$, while the EMEC covers the region $1.375 < |\eta| < 3.2$.

As briefly described in Chapter 2, the ATLAS EM calorimeter has alternating layers of lead absorbers and liquid argon (LAr) [9]. The lead material was chosen for its short radiation length ($X_0 = 0.57$ cm from Equation 3.1). This enables maximum shower containment while minimizing the geometrical size of the detector. It also uses a specially designed accordion geometry which allows full ϕ symmetry in terms of linearity and

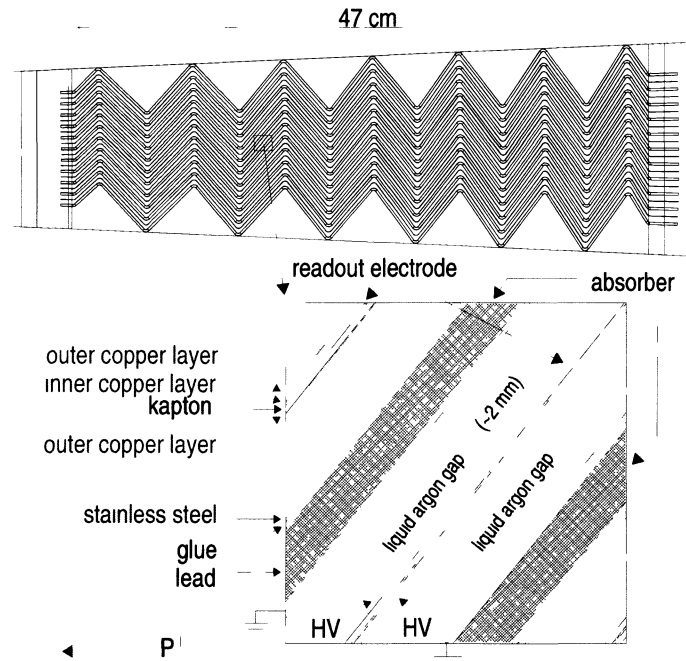


Figure 3.3: The overall and detailed view of the liquid argon calorimeter system in ATLAS. Figure from [16]

resolution.

Figure 3.3 shows the schematic drawing of the details of the accordion geometry and the alternating layout. The accordion waves axially in the barrel region and radially in the end-cap region. The folding angles in both regions vary with radius to keep the LAr gap constant. The lead absorbers have a different thickness depending on the location along η . For the EMB, the lead layers have a thickness of 1.53 mm for $|\eta| < 0.8$ and 1.13 mm for $|\eta| > 0.8$, and for the EMEC, the layers have a thickness of 1.7 mm for $|\eta| < 2.5$ and

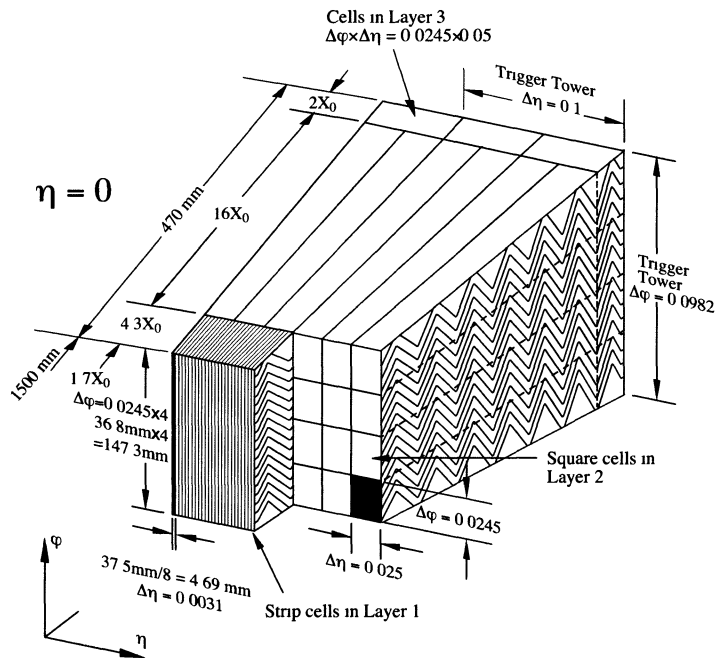


Figure 3.4: Schematic drawing of an EMB module. Figure from [9]

2.2 mm for $|\eta| > 2.5$. They are sandwiched with two stainless-steel sheets with thickness of 0.2 mm for mechanical strength. In the middle of the LAr gap are three readout electrodes (two outer layers maintained at 2000 V and inner signal readout) separated by a layer of kapton for insulation. The LAr gap is 2.1 mm on either side of the electrodes.

The LAr calorimeter components are divided into modules. The EMB is divided into two half-barrels, which is further divided into 16 modules, each covering the ϕ region $\Delta\phi = 22.5^\circ$. A schematic drawing of an EMB module is shown in Figure 3.4. Each module has a depth of at least $22X_0$ ($22 - 30X_0$ in the region $|\eta| < 0.8$ and $24 - 33X_0$ in the region $0.8 < |\eta| < 1.3$) in order to contain the full shower. The EMEC is divided

into 8 modules with a depth of at least $24X_0$ ($24 - 28X_0$ in the region $1.475 < |\eta| < 2.5$ and $26 - 36X_0$ in the region $2.5 < |\eta| < 3.2$).

In both cases, each module is also divided into three separate layers with different granularity. The first layer is finely segmented in η to provide precise position measurements, the second layer measures most of the EM shower energies, and the third layer provides the energy information in the tail of the EM shower. Table 2.1 details the granularity for each layer.

As mentioned previously, the EM calorimeter surrounds the ID system. Because particles must travel through ID material and the cryostat wall in order to get to the calorimeter system, there is a need to compensate for the energy lost by the particles before reaching the calorimeter. In ATLAS, this is done using a presampler, which covers the region $|\eta| < 1.8$. The presampler is a separate thin LAr layer which measures 11 mm in depth. See Table 2.1 for the granularity in the presampler.

The energy resolution of a calorimeter is given in Equation 2.1. In order to determine the resolution of the ATLAS EM calorimeter, a test beam analysis was performed, in which four EMB and three EMEC modules were subjected to electrons and positron beams. For the EMB, the beam energies ranged from 10 to 250 GeV at $|\eta| = 0.687$ [9], while for the EMEC the beam energies ranged from 10 to 200 GeV covering the entire EMEC η range ($1.375 < |\eta| < 3.2$) [17]. It was found that for the EMB the stochastic term in the resolution equation is $a = 10\% \cdot \sqrt{GeV}$ and the constant term is $b = 0.7\%$ [9]. These values are important for the work presented in Chapter 4.

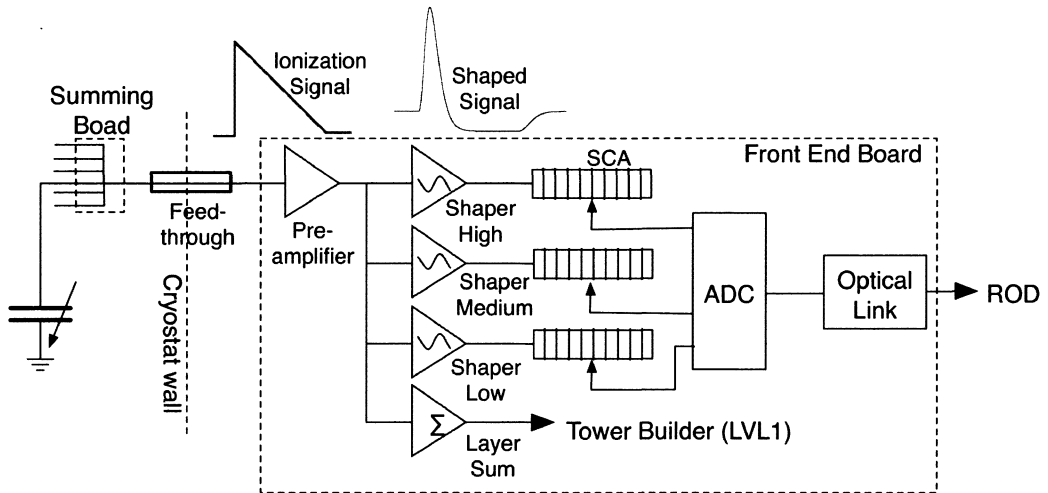


Figure 3.5: Schematic drawing of an FEB module. The high voltage enters via the feed-through and output is sent via optical link. Figure from [16]

3.3 Energy Reconstruction in the EM Calorimeter

An EM particle that traverses the EM calorimeter will deposit energy. From the signal collected by the calorimeter, its incident energy is reconstructed. This reconstruction is performed by components located on the Front End Board (FEB) [9, 18]. A schematic drawing of an FEB is shown in Figure 3.5. The method taken from the signal collection to the energy reconstruction is as follows.

Showered EM particles travel through the LAr gap which then ionizes the material. A high voltage induces a potential difference across the LAr gap. The electrons resulting from ionization then drift across the gap with drift time of about 450 ns at the operating voltage and they are collected by the electrode in the middle of the gap (Figure 3.6 - left), resulting in a triangular current pulse shape (Figure 3.6 - centre). The ionization

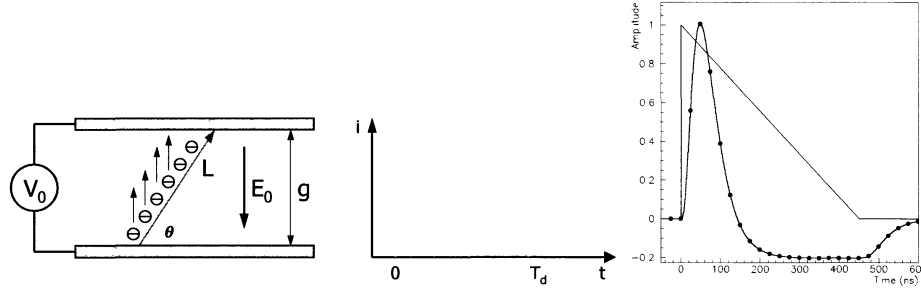


Figure 3.6: Left: The ionized electrons drift towards the signal electrode due to HV. Centre: The collected charge as a function of time. Right: Comparison of ionization signal and reshaped pulse. The digitization samples the pulse at 25 ns interval. Figures from [19]

signal is then transferred to the FEB through a Feed-Through (FT), which is a gateway between the detector module located inside a cryostat kept at the cold temperature of $T = 89$ K and FEB located outside the cryostat at room temperature.

The signal that arrives at the FEB is first amplified using a pre-amplifier and then shaped [9]. The shaper has three different gains (high, medium or low) depending on the strength of the incoming signal. The shaped signal has a peak followed by a negative trough (See Figure 3.6 - right) which compensates for the subsequent signals that can contribute to signal pile-up. The time of shaped signal is ~ 600 ns. The SCA (**S**witched **C**apacitor **A**rray) stores the analog signal until the trigger decision, at which point the signal is transferred to an ADC (**A**nalog to **D**igital **C**onverter) that converts to digital signal sampled at the LHC bunch crossing interval of 25 ns. The digitized signal is finally read out through an optical link.

Using $N_{samples}$ samples (typically five) of signal s_j that are taken from the peak region

of the shaped pulse, cell-level energy is reconstructed as follows [16, 19]:

$$E_{cell} [MeV] = (F_{\mu A \rightarrow MeV} \cdot F_{DAC \rightarrow \mu A}) \cdot \frac{1}{\frac{M_{phys}}{M_{cal}}} \cdot \sum_{i=1}^{M_{ramps}} R_i \left[\sum_{j=1}^{N_{samples}} a_j (s_j - p) \right]^2. \quad (3.6)$$

$F_{\mu A \rightarrow MeV} \cdot F_{DAC \rightarrow \mu A}$ is the analog to digital conversion factor. It is a product of the sampling fraction ($F_{\mu A \rightarrow MeV}$) and the conversion from the local DAC units to μA ($F_{DAC \rightarrow \mu A}$). These values are obtained from Monte Carlo studies and beam tests. M_{phys}/M_{cal} is the ratio between the maximum amplitude of the real signal and the maximum amplitude from the calibration signal. Figure 3.7 shows the comparison of real signal and the calibration signal. The summed terms are the signal samples s_j corrected for the baseline offset p (called the pedestal). The corrected signal sample calculation requires the ADC to DAC conversion gain (also known as ramps R_i), and Optimal Filtering Coefficients (OFCs) a_j [19, 18]. The OFC are the coefficients used to estimate the peak amplitude and the starting time of the signal while minimizing the noise. In practice, there is no non-linearity in ADC to DAC conversion for ATLAS calorimeter, so $M_{ramps} = 1$. These coefficients are obtained from calibration runs and updated on regular basis. See the next section for more details on some of these terms.

From the cell energy, the total electron energy is computed by adding up contributions from energy deposited in front of the calorimeter (determined from the presampler), the energy deposited in the calorimeter, and energy deposited outside of the calorimeter (longitudinal leakage). This method is known as the ‘‘calibration hits’’ method, and the addition is done as follows [20]:

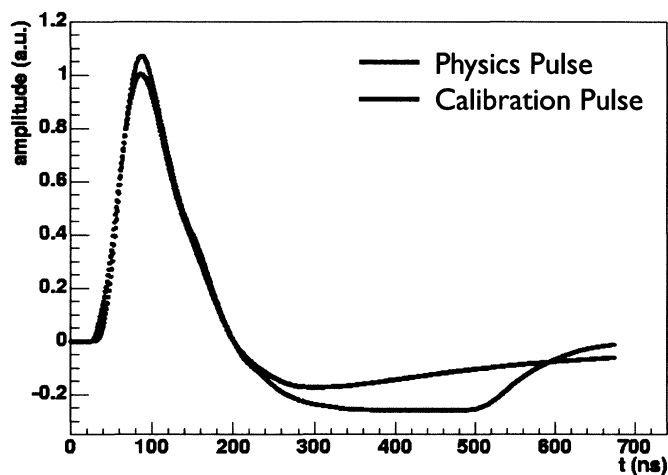


Figure 3.7: Example signal pulse for calibration (black) and physics (red). Figure from [16]

$$E^{reco} = (a + bE_{PS} + cE_{PS}^2) + \left(\frac{s_{cl}}{f_{out}} \sum_{i=1}^3 E_i \right) \cdot (1 + f_{leak}) \cdot F, \quad (3.7)$$

where:

- E_{PS} and E_i are energy measured in the presampler cluster and i -th layer of calorimeter (where $i = 1, 2, 3$) respectively
- a , b , and c are parameters determined as a function of energy measured in the accordion layers of the calorimeter. The parameter a is called “offset” and b is called “slope”. In the barrel regions ($0 < |\eta| < 1.475$), there is no non-linear term ($c = 0$)
- s_{cl} is the correction factor to the sampling fraction in the cluster
- f_{out} and f_{leak} are lateral leakage (energy in the calorimeter outside the cluster) and longitudinal leakage correction, respectively

- F is the η and ϕ dependent energy correction factor that corrects for subtle detector imperfections.

The performance of this reconstruction method is quantified as a ratio of reconstructed energy and true energy, known as “linearity”. The linearity for electrons is within 0.5% for all energy scales [20].

3.4 Calibration of the EM Calorimeter

In order to correctly reconstruct the particle energy using Equations 3.6 and 3.7, the necessary calibration parameters must be known. Some of these parameters are obtained from calibration runs, and others are based on Monte Carlo studies or beam tests. Calibration runs are performed by sending a signal to the detector that mimics the triangular wave shown in Figure 3.6 - centre. This is repeated frequently (sometimes on a daily basis) to monitor the condition of the calorimeter and to update these parameters if they deviate by more than some predetermined threshold.

A calibration run consists of three separate stages: pedestal runs, delay runs, and ramp runs. Each measures different parameters needed for energy reconstruction.

In pedestal runs, the FEB are read with no input signal. The purpose of this type of run is to measure the signal’s baseline value (pedestal), the noise fluctuation, and the noise autocorrelation values between samples s_i . The pedestal value p is one of the terms needed in energy reconstruction (see Equation 3.6). The electronic noise contributes to the energy resolution as given in Equation 2.1. The autocorrelation is used for the computation of OFC a_j in Equation 3.6.

The delay runs extract a reconstructed pulse shape from an injected calibration pulse. The calibration pulse is an exponential current pulse rather than a triangular one, and it is generated using a series of circuitry on the FEB. This exponential shape has a direct consequence on the output pulse shape and the difference from a true physics pulse can be seen in Figure 3.7. The maximum peak value of the two pulse shapes are significantly different, and this difference gives rise to the term M_{phys}/M_{cal} in Equation 3.6. One can also notice the difference in the tails of the pulse. This pulse shape is also used in the computation of OFC a_j .

The ramp runs are responsible for finding the ADC to DAC gain slope. Because this relies on the peak value corresponding to a given DAC value, the OFC must be calculated beforehand. From this, the R_i parameter in Equation 3.6 is determined from a linear fit of the DAC value versus the ADC value.

Another important purpose of a calibration run is to find and keep track of misbehaving channels. In the LAr systems, there are approximately 180,000 readout channels, all of which are a part of a complex readout system. When any of these channels starts to misbehave, this may result in a mis-calculation of the energy. Some of these problems include increased noise, dead cell readings, misshaped signal, gain problems and stability problems.

The Ecal team is responsible for validation of each calibration run. For each of the calibration run stages described previously (i.e. pedestal, delay and ramp), the values are compared to that of a reference run. A reference run is a calibration run that was determined as a “normal” run with no unexplained problems. Those channels that deviate more than predetermined threshold are noted as potential problematic channels,

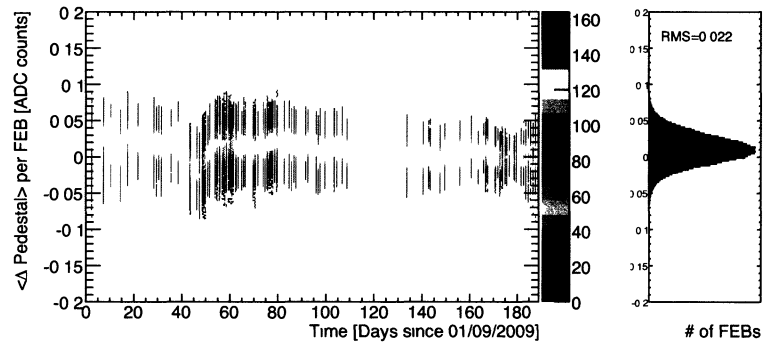
		Channel					FEB				
		Pedestal (ADC)	Noise (ADC)	Autocorr (abs)	Delay (%)	Ramp (abs)	Pedestal (ADC)	Noise (ADC)	Autocorr (abs)	Delay (%)	Ramp (abs)
EMB	H	1.5	0.8		10	0.015					
	M	0.9	0.2	0.05 (all)	4	0.004	0.2 (all)	0.05 (all)	0.04 (all)	5 (all)	0.004
	L	0.9	0.2		4	0.004					
EMEC	H	1.5	0.8		6	0.006				2	
	M	0.9	0.2	0.05 (all)	1.5	0.004	1.5 (all)	1 (all)	0.02 (all)	0.6	0.001
	L	0.9	0.2		1.5	0.004				0.6	
HEC	H	1.5	0.8		5	0.004					
	M	0.9	0.2	0.05 (all)	1	0.0015	1.5 (all)	1 (all)	0.02 (all)	3 (all)	0.001
	L	0.9	0.2		1	0.0015					
FCal	H	5	4		15	0.02					
	M	1.3	0.6	0.05 (all)	10	0.015	5 (all)	4 (all)	0.02 (all)	10 (all)	0.001
	L	1	0.2		10	0.015					

Table 3.1: Threshold values of calibration parameters used for validation. For each subdetector, there are different threshold values depending on the gain (High, Medium and Low), and depending on per channel or per FEB.

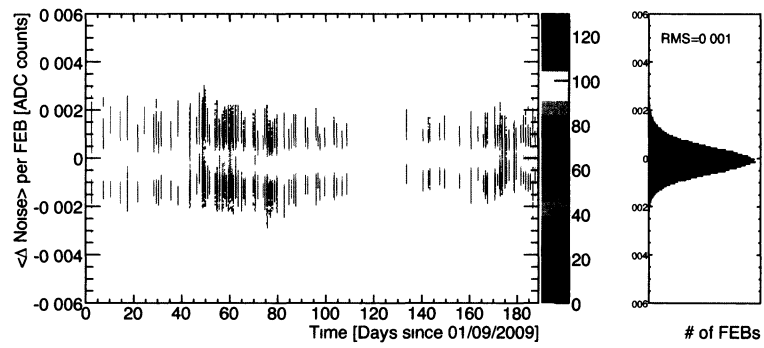
and they are masked or removed from the readout. The threshold values for which the parameters are classified as significantly deviated are presented in Table 3.1 [21]. This validation process is mostly automated, but the automation program needs to be maintained and checked for consistency. Its maintenance is another responsibility of the Ecal team. The detailed information about the validation process is presented in [22].

3.5 Stability Study of the EM Calorimeter

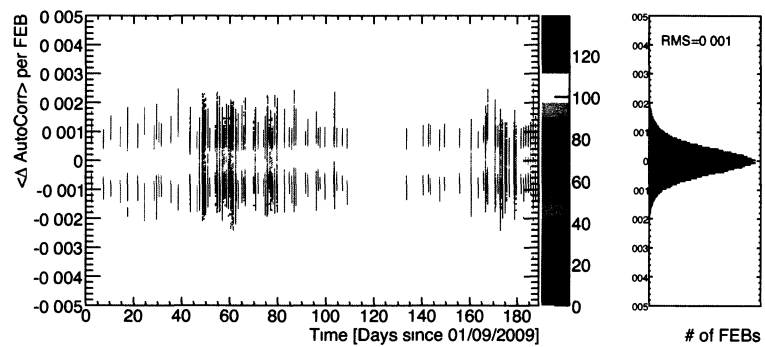
It is important that the performance of the calorimeter be stable and within expectations. Each calibration run is validated for problems by comparing to previous reference runs. However this may not be enough to discover possible subtle effects that may lead to miscalibration. An example of this is a slow drift of a parameter over time. For this reason, time stability studies were carried out on the individual components that make up the LAr calorimeter system.



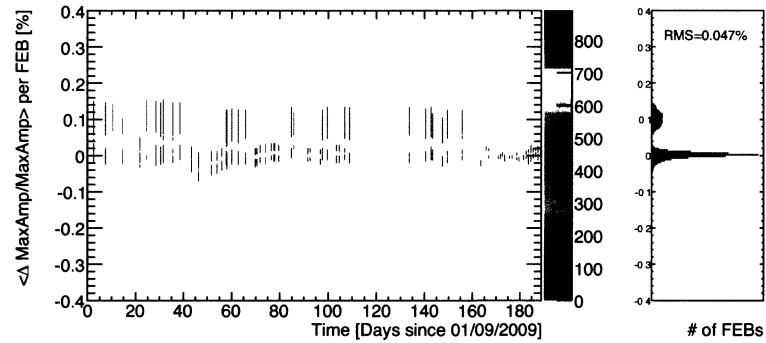
(a) Pedestal



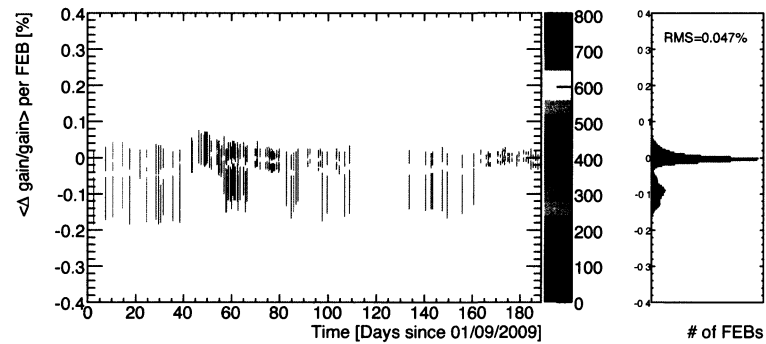
(b) Noise



(c) Autocorrelation



(d) Maximum amplitude



(e) Gain

Figure 3.8: Stability plots for combined EMB and EMEC as a function of time over a 180-day period in 2009. From (a) to (e): Stability of pedestal, noise, autocorrelation, maximum amplitude, and gain values.

The difference between each calibration run and the reference run is calculated and then plotted versus time. Figure 3.8 shows examples of stability plots over a 180-day period in 2009 for pedestal, noise and autocorrelation from pedestal runs, maximum pulse amplitude from delay runs, and gain from ramp runs for combined EMB and EMEC. Since for each run all of the parameters are compared at the FEB level, one can also see the spread of the differences. For each of the plots, there is a projected histogram on the right side depicting the spread for each run.

In the ideal case, the difference should be minimal. The difference should follow a Gaussian distribution with zero mean (such as the stability plot for the pedestal, noise and autocorrelation in Figure 3.8) and a width determined by the precision of the measurements. However, as it can be seen, this is not the case for some delay and ramp runs. Both exhibit some deviations from the reference (about 0.1% for delay and -0.1% for ramp). It is found that this is partially correlated to the status of the solenoid that surrounds the inner detector [22]. Because of the location of EMB, the magnetic field from the solenoid directly affects the signal. The opposite deviation of gain parameter can be explained by the fact that the gain parameter is anticorrelated with the maximum amplitude. These stability studies were done during the commissioning period when the status of the detector was not always stable. During the normal run conditions, the status of the detector components should remain unchanged (the solenoid, for example, should always be on).

Some preliminary studies have suggested the temperature of the FEB may also affect the stability of the calibration parameters [22]. However, due to other influences (such as those from magnetic fields), the effects due to temperature difference remain inconclusive.

Chapter 4

Calorimeter Energy Response Study

There is a dedicated working group within the ATLAS collaboration whose main tasks are identification and reconstruction of electrons and photons in the ATLAS detector [23]. The development of proper identification and reconstruction algorithms requires extensive knowledge of the electromagnetic (EM) calorimeter and the charged-particle tracker. One of the key ingredients in such algorithms is the energy measurement of the particle, and for this purpose the understanding of ATLAS EM calorimeter is especially important. In this study, several aspects of the energy response of the EM calorimeter are investigated using samples from Monte Carlo (MC) studies that simulate realistic particle interactions inside the ATLAS detector. Only electrons will be of concern for this study.

The ATLAS EM calorimeter is introduced in Section 3.2. In an ideal EM calorimeter, the reconstructed energy should reflect precisely the actual energy of the electron. If the reconstructed energy is not identical to the real electron energy, this has a direct impact

on the analysis of many of the more sophisticated physics interactions expected at the LHC. In reality, there are some factors that influence the energy reconstruction of the electrons in the ATLAS calorimeter. In this study, three of such factors are investigated. They are i) influence of simulation details, ii) influence of extra materials in the detector, and iii) influence of particle interactions with the detector.

4.1 Methodology

4.1.1 The Sample Datasets

The samples used for this study were leptonic W boson decay ($W \rightarrow e + \nu$) events produced using the ATLAS MC simulation chain. In ATLAS, this involves two major components [24]. First is the generation of primary particles by simulating the hard-scattering of the two colliding protons. This involves calculation of matrix elements of interacting quarks and gluons inside the protons as described by parton density function. Subsequent interactions create parton showers and they are grouped into composite hadrons (hadronization) via phenomenological hadronization models. Finally, decays of short-lived particles are simulated. This part of the MC is achieved with PYTHIA event generator [25]. The second component in the ATLAS MC simulation chain is the detector simulation. The particles produced by the generator will interact with the detector material following various models of propagation of particles through matter depending on the nature of the particle (electromagnetic or hadronic). The simulation model takes into account the material distribution and the geometry of the detector. It is able to keep track of particles through the detector using the underlying physics model (true

particle information) as well as realistic detector output. This part of the MC is done using GEANT4 package [26]. The simulated events are then digitized and reconstructed using the ATLAS-specific Athena software.

Since this study concerns itself with three different aspects, three independent MC datasets were used:

- **mc08 dataset:**

(mc08.106020.PythiaWenu_1Lepton.merge.AOD.e352_s462_r635_t53)

This dataset was generated by PYTHIA and reconstructed using Athena version 14.2.25. It contains 1 million $W \rightarrow e + \nu$ events. The standard ATLAS geometry package was used for this dataset (ATLAS-GEO-02-01-00), which models the realistic features of the complete detector.

- **mc09_valid dataset:**

(mc09_valid.106020.PythiaWenu_1Lepton.recon.AOD.e352_s462_s520_r729)

This uses the same PYTHIA-generated events as mc08, but reconstructed using the newer version of Athena (version 15.3.0). This dataset contains 750,000 $W \rightarrow e + \nu$ events. The geometry package was identical to that of the mc08 dataset (ATLAS-GEO-02-01-00).

- **mc09_valid distorted dataset:**

(mc09_valid.106020.PythiaWenu_1Lepton.merge.AOD.e352_s564_s584_r810_r816)

This dataset uses the same generated events as above (1 million $W \rightarrow e + \nu$ events), reconstructed using Athena version 15.3.1, and includes the artificially introduced extra material in the specific parts of the detector (ATLAS geometry package ATLAS-GEO-06-01-00) to study the effect of such geometry modification. The details of this modification will be discussed in Section 4.3.

4.1.2 The Selection Requirements

Even in MC datasets, there are many events that do not have relevance to this study because PYTHIA produces W bosons of all energies that interact realistically with the detector material. In order to minimize the influence of these unwanted events, several selection requirements were introduced to ensure the quality of the sample.

- **Loose electron requirement:** Within the reconstruction algorithm, the electrons are identified using only the calorimeter information, primarily shower shape information from the second layer of the EM calorimeter (Refer to Section 5.1.2 for more detail). The loose selection will enrich the electron samples in the dataset without being too restrictive in its selection method. This will maximize the number of electrons in the dataset and thus improves the statistics needed for the study.
- **Momentum requirement:** Only electrons with transverse momentum greater than 20 GeV are used for the study. This will match the realistic situation of the data samples for $W \rightarrow e + \nu$ because there is an applied 20 GeV electron trigger.
- **Pseudorapidity:** Only events within the region of pseudorapidity $|\eta|$ less than 2.5 are used. This corresponds to regions in the detector with tracking capability and thus reflects the region where standard electrons can be identified.
- **Remove crack region:** The crack region is defined as the transition region from barrel to end-cap EM calorimeter ($1.37 < |\eta| < 1.52$). This region is known to have an extensive amount of inactive (or dead) material due to service cables and support structures. Therefore the resolution is poor in this region.

4.1.3 Energy Response Distribution as a Study Parameter

One of the important and useful parameters to quantify the quality of a calorimeter is the energy response, defined as $E^{\text{reco}}/E^{\text{truth}}$. E^{reco} is the energy of the reconstructed electron,

and E^{truth} is the true energy of the electron extracted from Monte Carlo simulations. The energy response quantifies how precisely the calorimeter can measure the real energy, and for an ideal calorimeter this quantity should be equal to one. For the ATLAS EM calorimeter, it is required that the mean energy response is no more than on the order of $\sim 0.1\%$ away from one. This is imposed due to the desired precision of measurements such as the mass of W bosons.

Figure 4.1 (left) shows a typical energy response distribution for electrons. As one can see, the distribution has a Gaussian peak at around one, but it has asymmetrical tails on both the high ($E^{\text{reco}}/E^{\text{truth}} > 1$) and the low ($E^{\text{reco}}/E^{\text{truth}} < 1$) sides. There is an obvious tail in the low region and less obvious tail in the high region. These tails are suspected to be influenced by particle interactions with the detector such as bremsstrahlung. In the absence of such interactions, the response should resemble the Gaussian core region of the distribution. The width of the distribution is mainly due to the resolution effects of the detector. Also, the energy response is expected to be uniform in pseudorapidity η for an ideal calorimeter.

4.1.4 The Fitting

As mentioned above, the energy response of the calorimeter ($E^{\text{reco}}/E^{\text{truth}}$) has a core region and a tail region. Since the peak of the distribution defines the response of the calorimeter, it is essential that the calculation of the peak of the distribution not be influenced by the non-Gaussian tails.

One effective way to limit these effects is to use a fitting method that iteratively decides and separates the “core” and “tail” using mean and width information from each

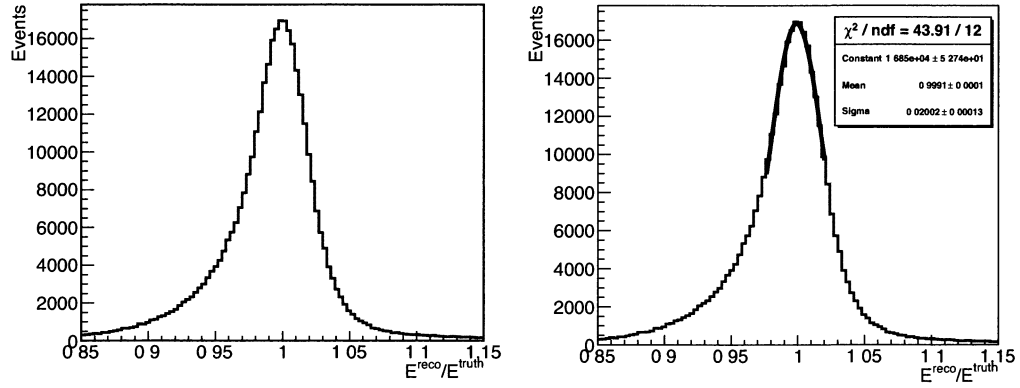


Figure 4.1: An example of energy response distribution for reconstructed electrons from $W \rightarrow e + \nu$ decay in the ATLAS detector. The right shows a typical result from the fitting procedure.

fit. The steps involved in this method are as follows:

1. Fit to a Gaussian distribution through the entire range using 80 bins in the range $0.9 < E^{\text{reco}}/E^{\text{truth}} < 1.1$. The Gaussian fitting is used because it is expected that the energy response distribution in the core would follow a normal distribution. From the fit find the mean μ and the width σ
2. Redo the fit, but use range $\mu \pm \sigma$ from previous step. It is assumed that the tail has little effect in this range and this separates the distribution into core and tail regions.
3. Repeat the fit once more. This will readjust the mean and the width that might not have been accurately calculated in the previous step.

A typical result of this fitting procedure is depicted in Figure 4.1 (right). As it can be

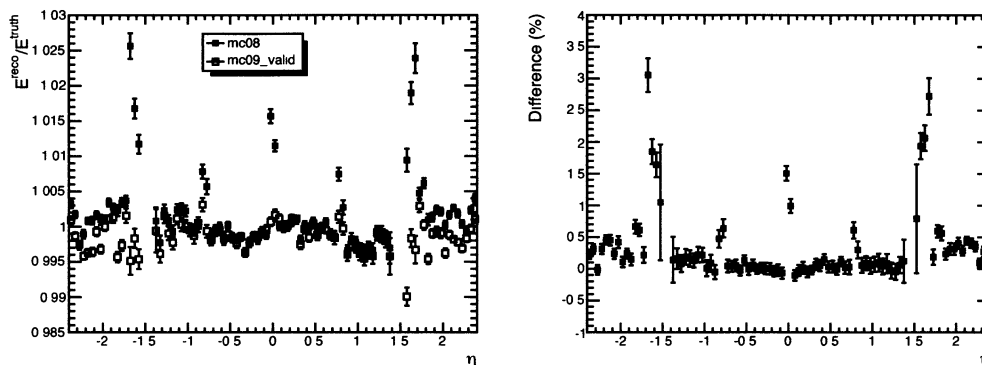


Figure 4.2: Left: The calorimeter energy response for reconstructed electrons using Athena version 14 (mc08 - black/filled) and version 15 (mc09_valid - red/open). Right: The percent difference in energy response between the two versions (mc08 - mc09_valid).

seen, the fit estimates the peak of the distribution with reasonable accuracy.

4.2 Comparison of Athena 14.2.25 Version and Athena 15.3.0 Version

Simulation-based analyses are an essential component in particle physics, and many of these analyses are sensitive to the subtle details in the simulation. For this reason, the ATLAS software framework, Athena, is subject to regular updates. These updates may include improved reconstruction algorithms and calibration constants, hence the results of the simulation may not be identical from one version to the next. The goal of this section of the study is to identify any impact on the energy response as a result of the software upgrade from version 14.2.25 (mc08) to 15.3.0 (mc09_valid).

An earlier version of Athena, version 14.2.25, was used to reconstruct the electrons in

the mc08 dataset, and it uses an older version of reconstruction method (more specifically, calorimeter cluster correction version v5_calh). After some investigation, it is found that this algorithm included an unintentional calculation error that affected energy response at transition η regions in the barrel calorimeter. As one can see from Figure 4.2 (left), which plots the mean of the fit, jumps in mc08 (black/filled points) can be seen at $\eta = 0$ and at $|\eta| = 0.8$ (jumps at $|\eta| \sim 1.6$ are due to resolution problems near the crack regions). On the other hand, the more recent version of Athena, version 15.3.0, uses the updated version of reconstruction method (v6_calh), which consequently fixes the aforementioned calculation error which are related to miscalculation of barycentre in the transition zone [27]. It can be seen that for both datasets, the energy response in the central region ($|\eta| < 1.0$) is within 0.5% away from one. Figure 4.2 (right) depicts the percent difference of distribution and clearly points out the η dependent bugs in version 14.2.25. Note that apart from these problematic regions, the overall difference is within 0.5% level.

The details of the impact due to these errors can be seen in Figure 4.3. The left plot shows the distribution at $\eta = 0.2$, where there were no calculation errors and therefore no significant difference is observed. The middle plot shows the distribution at $\eta = 0$. As one can see, the miscalculation in mc08 introduces a bump to the right of the peak, which is fixed in mc09_valid. Finally, the error at $\eta = 0.8$ is visible on the right plot. The mc08 distribution peaks at significantly different value and also slightly wider than mc09_valid.

Figure 4.4 shows the comparison of energy response core distribution width as a function of η for both Athena versions (black/filled is mc08 and red/open is mc09_valid),

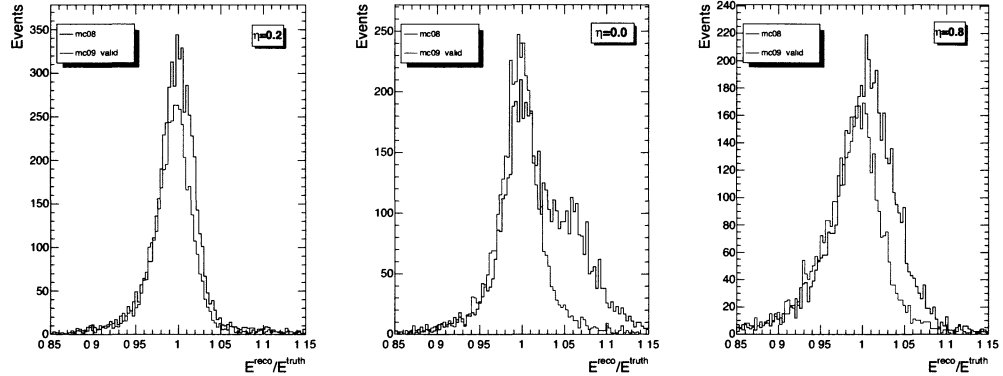


Figure 4.3: Energy response distribution for mc08 (black) and mc09_valid (red) at specific η . Left is at $\eta = 0.2$, middle is at $\eta = 0.0$, and right is at $\eta = 0.8$.

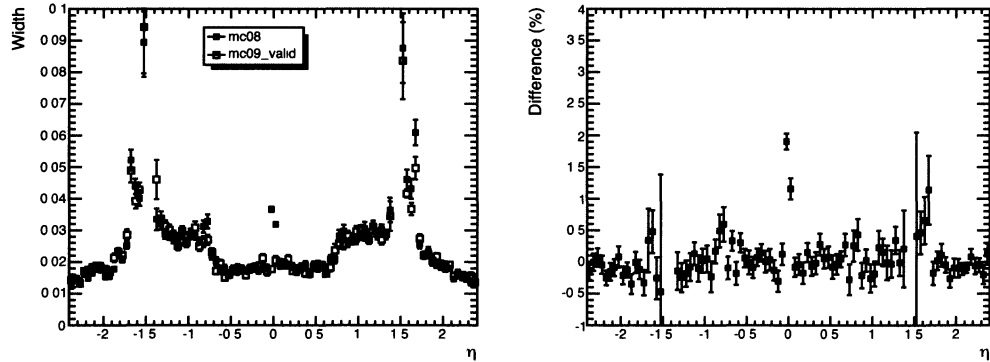


Figure 4.4: Left: The energy response distribution core width (standard deviation from the fit) for reconstructed electrons using Athena version 14 (mc08 - black/filled) and version 15 (mc09_valid - red/open). Right: The percent difference in the width between the two versions (mc08 - mc09_valid).

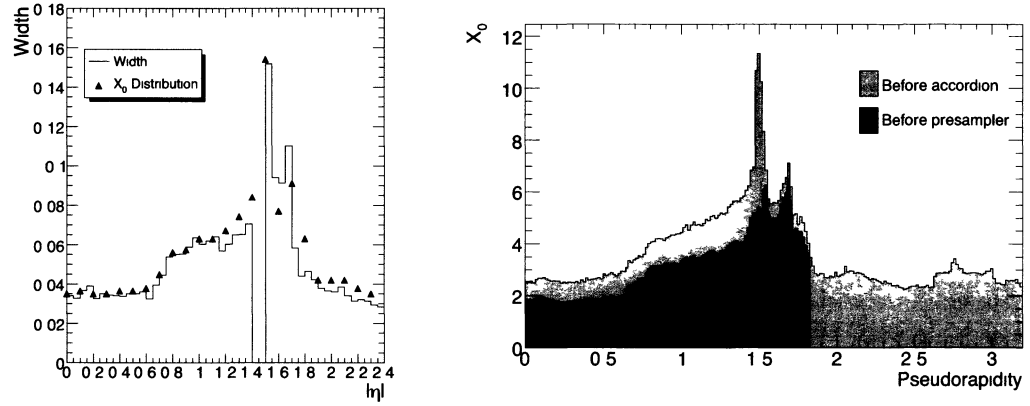


Figure 4.5: The energy response distribution core width (standard deviation from the fit) for reconstructed electrons as a function of absolute η overlaid with the amount of material measured in radiation length X_0 located in front of the EM calorimeter before the accordion structure (right figure from [9]).

where the width is defined as the standard deviation from the fit. It is clear that there is no observable difference in the width between the two versions with exception at $\eta \approx 0$. The width plotted as a function of η has a unique feature that it jumps at $|\eta| \sim 0.8$ and again near the crack region before it drops in the end-cap region. It is strongly correlated to the material distribution measured in radiation length X_0 in front of the EM calorimeter. As one can see from Figure 4.5 (left), the agreement of the width with the material distribution in front of the EM calorimeter before the accordion structure as a function of η as shown in Figure 4.5 (right) is good. As it will be discussed in detail later, the width of the response distribution is influenced by the incoming particle (in this case an electron) interacting with the detector, therefore the agreement as seen in Figure 4.5 is not very surprising.

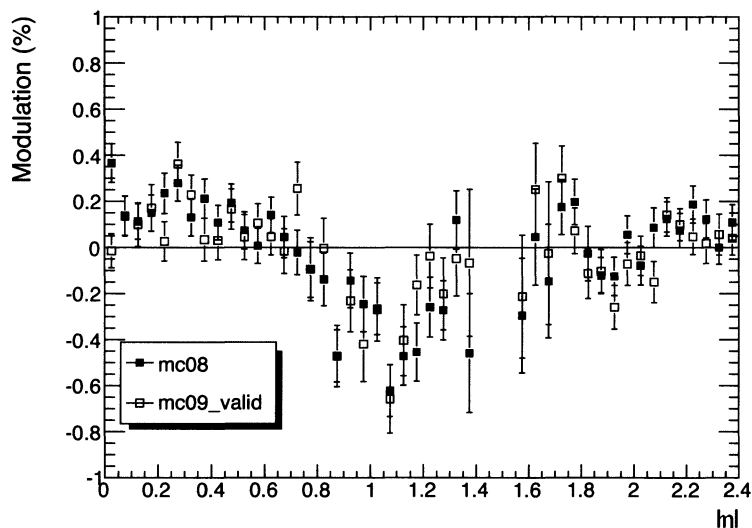


Figure 4.6: The η distribution of the modulation for calorimeter energy response.

It has already been mentioned that the energy response in an ideal calorimeter should be η independent and η symmetric. In order to verify this hypothesis in the ATLAS calorimeter, the η asymmetry (Modulation) is calculated, which is the difference in energy response between the negative and positive η . That is, for the k -th η bin:

$$\frac{E^{\text{reco}}}{E^{\text{truth}}}(\eta = k) - \frac{E^{\text{reco}}}{E^{\text{truth}}}(\eta = -k). \quad (4.1)$$

The resulting plot expressed as a percent difference is depicted in Figure 4.6. A modulation can clearly be seen in both versions of reconstruction, which shows an oscillating feature. It is found that this is an effect from an algorithm in the simulation that mimics the 0.7% constant resolution term in the ATLAS EM calorimeter (See Equation 2.1) [9].

This imperfection was artificially introduced in the simulation since the simulation output by itself results in a significantly lower constant term. This is done by introducing region-to-region spread of the energy in $\eta - \phi$ space. Because this method has finite regions, the statistical fluctuation at the same η but different ϕ may be different, which consequently creates deviations that do not average to zero [28].

4.3 Material Distortion

The ATLAS EM calorimeter consists mainly of lead and liquid argon. However, there also exist other materials that are necessary for its operation. Such materials include cables for power and data transmission, and support structures that hold the calorimeter in place inside the detector. These materials, however, are not part of the calorimeter, hence they may affect the performance of the active component of the calorimeter, since the particles may interact with these non-active (or dead) materials. The official ATLAS MC simulation already includes these imperfections, but the level of accuracy of this simulation still remains to be verified with real data.

In order to investigate the influence of such imperfections, a separate MC study was carried out, in which the detector material distribution was modified in such a way that additional amounts of dead materials were included. Figure 4.7 shows the geometry set-up for such MC simulation. The detector was divided into quadrants in ϕ space, in both negative and positive η , and extra material was artificially inserted to each of the quadrants in specific location. For simplicity, only three cases were considered where extra material was added in only one part of the detector to see how it affects the energy

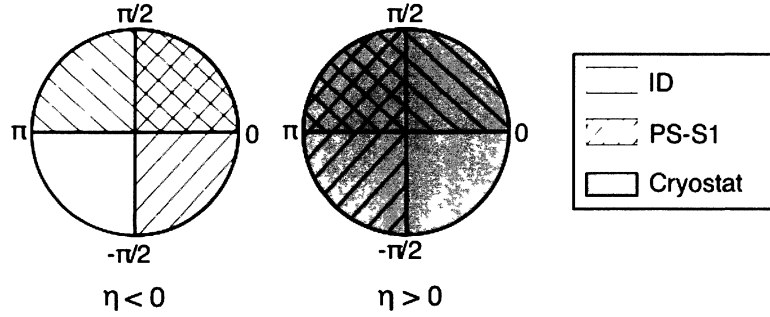


Figure 4.7: The setup of the MC simulation with distorted material. Additional materials were artificially inserted in each of the quadrants. [29]

response of the electrons in the calorimeter: i) Extra material added in the inner detector ($\eta < 0$ and $\pi/2 < \phi < \pi$); ii) extra material added between the pre-sampler and the first layer of the calorimeter ($\eta < 0$ and $-\pi/2 < \phi < 0$); and iii) extra material added in the cryostat ($\eta > 0$ and $-\pi/2 < \phi < 0$). The same analysis method as previously explained was used to find the energy response for this part of the study.

Figure 4.8 shows the distribution shape for normal geometry, where no extra material was added (black histogram: $\eta < 0$ and $-\pi < \phi < -\pi/2$, see Figure 4.7) and compares to that of distorted geometry (red histogram) all plotted at $|\eta| = 1.1$. As it can be seen, the ID distortion (left) has the biggest impact, while the PS (middle) and cryostat (right) distortion has less impact on the shape and the peak. Figure 4.9 shows this impact as a function of η over the full range. For each of the points, the energy response was separately fitted, and the mean of the fit in the quadrant with no extra material was subtracted from that of the distorted quadrant to show the difference in the response. The existence of extra material has small effect on the energy response up to $\eta \sim 0.8$, but

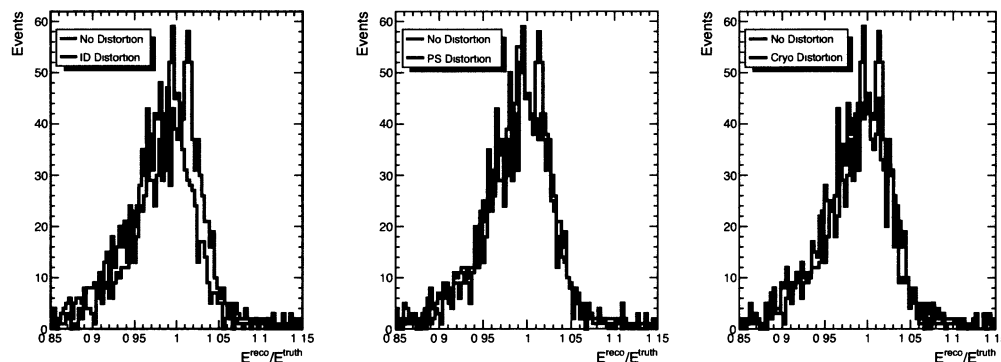


Figure 4.8: The impact of extra material on energy response at $|\eta| = 1.1$. The left is ID distortion, middle is PS distortion, and right is cryostat distortion.

beyond that the difference starts to become noticeable. In particular, the ID distortion has the biggest impact, as observed in Figure 4.8. The right plot of Figure 4.9 shows the width of the distribution and it is barely affected by the inclusion of extra material.

Explanation for the deviation beyond $\eta \sim 0.8$ could be found in Figure 4.10, which shows the added materials inside the inner detector. As one can see from the drawing, there is an extensive amount of added material starting from $\eta \sim 0.8$ (the vertically added material in the TRT). The material existent here creates additional premature EM showers before the calorimeter. In this situation, the calorimeter is not able to observe the full energy of the shower (details will be given in the subsequent section), thus lowers the reconstructed energy of the initial electron.

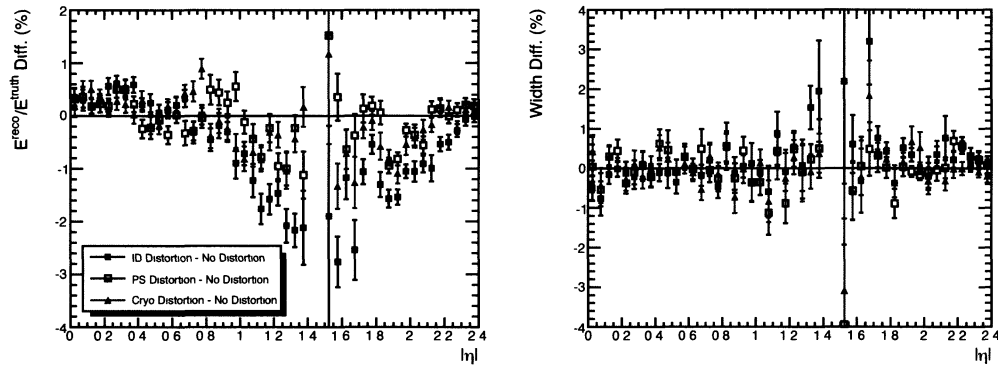


Figure 4.9: The impact of material distribution on the calorimeter response. Left: Difference in the mean of the response compared to that with no distortion. Right: Difference in the width of the response distribution.

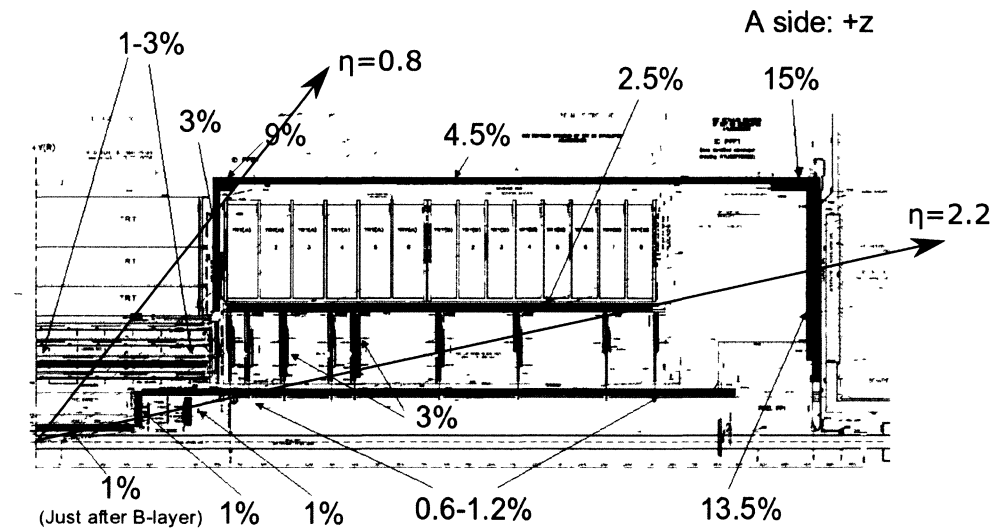


Figure 4.10: The cross section of distorted material distribution for the inner detector in the MC simulation. The red filled areas are the location of added material. [30]

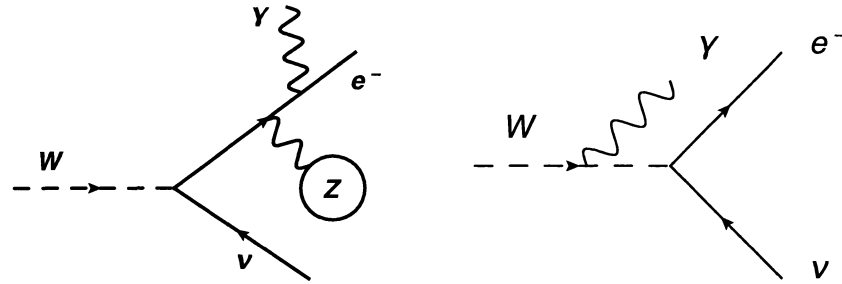


Figure 4.11: Two possible scenarios for bremsstrahlung of $W \rightarrow e + \nu$ decay. The left is external bremsstrahlung via Coulomb interaction with nearby nucleus with atomic number Z and the right is internal bremsstrahlung.

4.4 Study of Bremsstrahlung Effects

The last aspect of the investigation is the tails of the energy response distribution. As mentioned before, a well behaved particle detected by an ideal calorimeter is expected to have a Gaussian response. However in reality, the distribution has tails that distort the Gaussian distribution. These are mainly due to particle interaction and bremsstrahlung has a big impact. In the context of W boson decays, external bremsstrahlung refers to that of the electron from the decay of the W boson (see Figure 4.11 - left). In this process, the electron interacts with the Coulomb field of a nearby nucleus, and a photon escapes with some energy that may not get detected in the same calorimeter cluster. When the calorimeter information is used to reconstruct the electron, it does not associate the photon to the electron, therefore the reconstructed electron will have lower energy. On the other hand, internal bremsstrahlung refers to that of the W boson decay before it decays to electron and neutrino (see Figure 4.11 - right). In this process, the photon

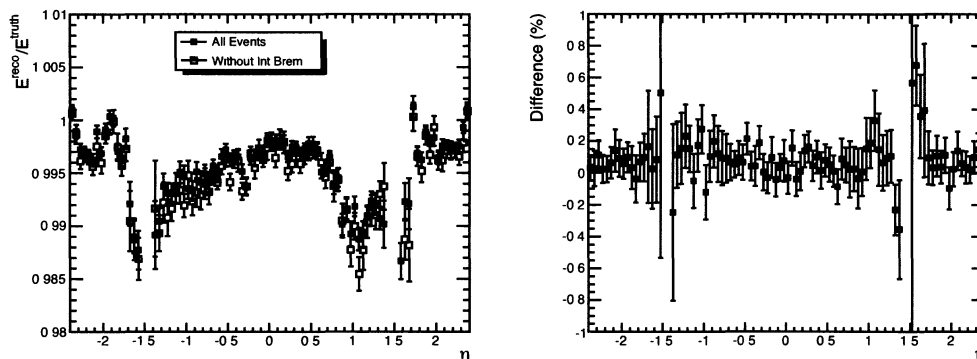


Figure 4.12: Left: Comparison of the calorimeter energy response with (black/filled) and without (red/open) the effect of internal bremsstrahlung. Right: The percent difference in energy response (All Events - Without Int Brem).

carries away energy along with the electron after the decay. However, it may have the same direction as the electron, and as a consequence it may get detected in the same calorimeter cluster. The calorimeter cluster will detect the energy of the electron *plus* the energy of the photon, therefore increasing the reconstructed electron energy.

The effects of external bremsstrahlung have been previously studied extensively, but less effort is invested in the studies of the effects of internal bremsstrahlung. Figure 4.12 shows the effect of internal bremsstrahlung on the energy response using mc09-valid MC dataset. It can be seen that the effect of internal bremsstrahlung is minor but the energy response decreases if the contribution of the internal bremsstrahlung is omitted (red/open points). Figure 4.12 (right) shows the percent difference. It can be seen that this affects the response by $\sim 0.1\%$.

Figure 4.13 (left) shows the energy response of events having these different bremsstrahlung types. It is clear that without the influence of bremsstrahlung events, the

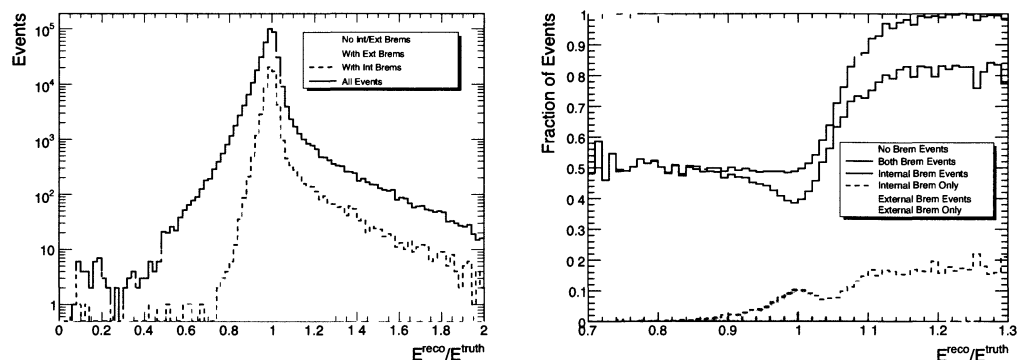


Figure 4.13: Energy response distribution by bremsstrahlung type. The filled histogram is the response without any bremsstrahlung events. Left plot shows the peak response range from 0 to 2 (note the logarithmic scale on vertical axis). Right plot shows the details in the range 0.7 to 1.3 as a fraction of total events in each bin.

distribution resembles a Gaussian. However, once bremsstrahlung events are added to the signal, this introduces non-Gaussian tails. From the right plot in Figure 4.13 which shows the fraction of events, one can see that the far tail region ($E^{\text{reco}}/E^{\text{truth}} < 0.8$ and $E^{\text{reco}}/E^{\text{truth}} > 1.2$) are purely bremsstrahlung events.

Figure 4.14 shows the fraction of events that are in the tail region of the energy response distribution as a function of η , where the plot on the left shows the tail regions. The low and high tails are defined as events with energy response 5σ lower and higher than the mean response, respectively, where σ is obtained from the Gaussian fit separately applied for each η bin. One can see that the distribution is uniform in η for the high tail. This is consistent with the results shown in Figure 4.13, that events in this region are due to internal bremsstrahlung. Because the W boson is such a short-lived particle, the bremsstrahlung from it occurs before it has time to travel through the detector material, so this type of events are expected to be isotropic. On the other hand, for low tail

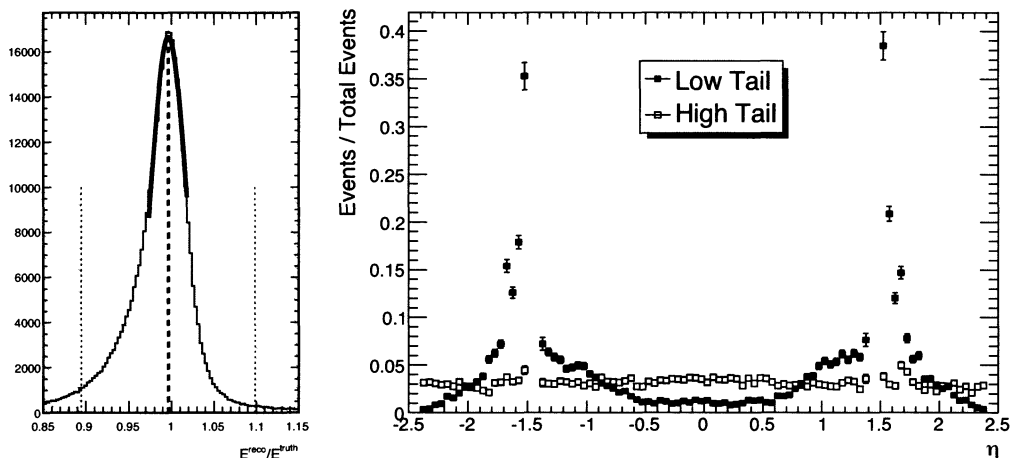


Figure 4.14: Fraction of events in the tail of the energy response distribution as a function of η . The left plot shows the region defined as “tail” of the distribution.

(black/filled points) the fraction of events is not uniform in η and increases near the crack regions. This also verifies the results in Figure 4.13, because the bremsstrahlung of electrons is a direct consequence of it interacting with detector material, therefore correlated to amount of material in their path. Because there is significantly more material near the crack region (see Figure 4.5), there are more occurrences of external bremsstrahlung in this region.

4.5 Summary

Three main topics concerning the quality of electron identification and reconstruction in the ATLAS detector were investigated using the energy response of electrons from leptonic W boson decays. The Monte Carlo simulation datasets were used to do the

analysis, which include both the reconstructed variables and truth variables, and a three-step Gaussian fit was employed in order to effectively carry out the analysis.

By comparing the simulation results between different Athena versions, it is found that subtle details within the simulation introduces observable differences. Some of them are related to unintentionally-introduced errors, and others are intentionally inserted to mimic a realistic detector.

The additional material in the detector is another factor that affects the energy response. It is found that the energy response is most sensitive to extra material added in the inner detector, and only beyond $\eta \sim 0.8$, given the geometry of the extra material in this simulation. The width of the energy response is not sensitive to the presence of extra materials.

Lastly, the impact of internal and external bremsstrahlung was studied in the tail region of the distribution. In the context of leptonic W boson decay, the internal bremsstrahlung gives a subtle rise to the tail in the higher response while the lower response tail is due to the external bremsstrahlung events.

Chapter 5

Electron Performance and W Boson Searches with Early Data

The LHC was successful in producing its first stable proton beams in September 2008. However it failed to collide the two beams due to a defect in the accelerator magnet system. This defect was responsible for a shut-down period lasting until November 2009, when the operation restarted and delivered its first very anticipated proton-proton collisions.

Since this restart of the LHC, ATLAS has acquired sufficient collision events for its first evaluation of the performance of the detector using electrons produced from these collisions. These electrons, in conjunction with the previous studies such as ones described in Chapters 3 and 4, can provide valuable information about the performance of the detector. ATLAS also collected collision data at the highest collision energy so far produced in a laboratory, which enables some preliminary physics analyses already at

this stage. However, it is limited to analyses involving high cross-section processes due to the low integrated luminosity.

The collision energy was kept at $\sqrt{s} = 900$ GeV towards the beginning of the collision runs as a part of a commissioning phase, since this corresponds to the beam energy of 450 GeV as it is injected into the LHC main ring (see Section 1.2.1). LHC delivered stable beams at this energy for a couple of months before the maintenance shut down to prepare for higher energy collisions. On March 30, 2010, the first collision at $\sqrt{s} = 7$ TeV was delivered.

During the first two-month period of the 7 TeV collision campaign, a small team was formed to analyze W boson candidates in new collision runs. I was involved as a part of this team to quantify properties of these W boson candidates as well as a part of a working group for the observation of W and Z bosons via the electron decay channel, the results of which are presented in this chapter.

In this chapter, electron properties at the collision energies of 900 GeV and 7 TeV are presented. In addition, some candidate W boson decays involving electrons in the final state were identified and analyzed in early 7 TeV collisions at ATLAS, and their properties are presented. The analyses presented here correspond to the accumulated collision data of integrated luminosity $\mathcal{L} = 9 \mu\text{b}^{-1}$ at $\sqrt{s} = 900$ GeV taken between November and December, 2009 (~ 380 thousand events) [31] and of integrated luminosity $\mathcal{L} = 1.0 \text{ nb}^{-1}$ at $\sqrt{s} = 7$ TeV taken between March and April, 2010 (~ 2.75 million events) [32]. ATLAS continues to take collision data at this energy scale, and is expected to continue doing so until the end of 2011.

5.1 Electron Candidates in Early ATLAS Data

Electrons are arguably the most familiar of the fundamental particles that are described by the Standard Model (Refer to Figure 1.1). They are also an abundant and integral part of many of the important and interesting interactions at ATLAS at all energy scales. Such examples include the Higgs boson decay ($H \rightarrow Z + Z \rightarrow e + e + e + e$), as well as the W bosons mentioned throughout this thesis work ($W \rightarrow e + \nu$). Therefore, it is crucial that the ATLAS detector be able to identify these electrons in the collision events in an efficient and accurate manner.

5.1.1 Kinematics Properties of Electron Candidates

The ATLAS electron identification algorithm is designed to identify high E_T electrons from primary physics interactions such as W and Z decays. For instance, electrons from such decays have transverse energy peaking at around 40 GeV. The early running data presented here at 900 GeV and at 7 TeV are mainly from QCD processes (due to their high cross-sections) and thus results in lower energy particles with few high energy electrons from primary processes. However, these data can still provide information on the performance of this electron identification algorithm, as well as an indication of the level of understanding of these interactions with the detector material.

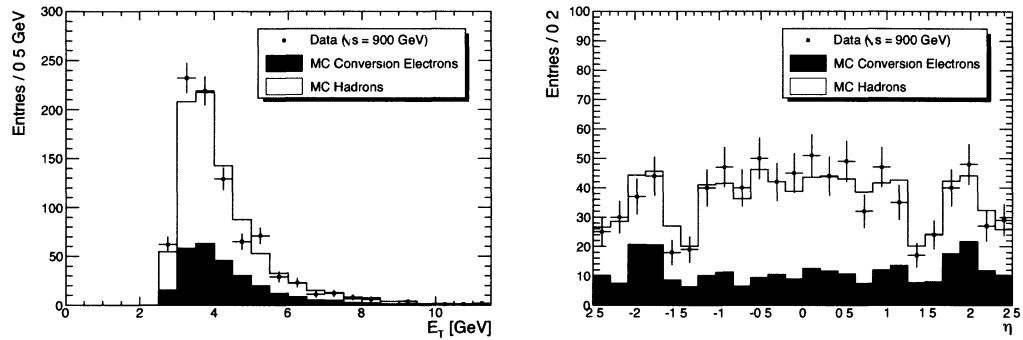
Since the Monte Carlo (MC) simulation in ATLAS takes into account of the expected detector effects, if the detector is well understood, then these simulated events should match the data when making the comparison between the data and the simulation output. For this part of the analysis, two separate MC samples are used, each corresponding to

two collision energies in the early data. Each sample is generated using PYTHIA [25] and full detector simulation was carried out using GEANT4 simulation package [26]. Each sample contains 10 million and 5 million non-diffractive minimum bias events for 900 GeV and 7 TeV collision energy, respectively. The dataset names are:

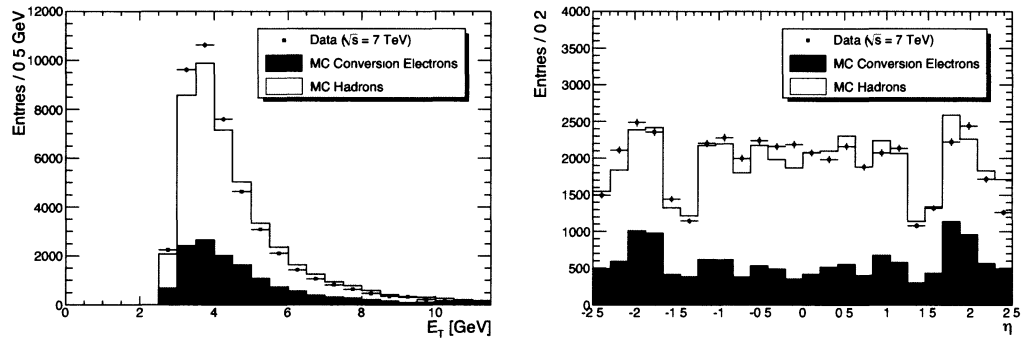
- **900 GeV Dataset (1 million events):**
(mc09_900GeV.105001.pythia_minbias.recon.e500_s655_d257_r1023)
- **7 TeV Dataset (500 thousand events):**
(mc09_7TeV.105001.pythia_minbias.recon.e468_s624_s633_r1064)

Before making the comparison to the collision data, several selection requirements are applied in order to ensure the quality of the data and enhance the probability that these particles are electrons:

- The collision events must be produced in a stable beam condition and under normal detector operational conditions;
 - The particle is identified as an electron by the default ATLAS identification algorithm. This algorithm starts with seed energy deposit $E_T > 2.5$ GeV in the second layer of the EM calorimeter. Then it finds the energy cluster using a sliding window technique with window size of $\Delta\eta \times \Delta\phi = 3 \times 5$ cells, where each cell in the calorimeter has size of $\Delta\eta \times \Delta\phi = 0.025 \times 0.025$. Subsequently a track matching the identified cluster is found by extrapolating the tracks found in the ID with momentum $p_T > 0.5$ GeV [31, 32];
 - The particle is within the pseudorapidity range dedicated to precision physics ($|\eta| < 2.47$), but remove the transition region from the barrel to endcap calorimeter ($1.37 < |\eta| < 1.52$);
 - The transverse energy of the particle E_T must be at least 2.5 GeV.
-



(a) Kinematics properties at 900 GeV.



(b) Kinematics properties at 7 TeV.

Figure 5.1: Kinematics properties of electron candidates. Left: Electron transverse energy profile E_T . Right: Pseudorapidity profile η

Figure 5.1(a) and Figure 5.1(b) show the distribution of transverse energy E_T and pseudorapidity η of the electron candidates collected from collision runs at the centre-of-mass energy of $\sqrt{s} = 900$ GeV and $\sqrt{s} = 7$ TeV, respectively. The data collected for the 900 GeV analysis contain 879 electron candidates after the selection described above. The data collected for this stage of the 7 TeV analysis are only up to integrated luminosity of $\mathcal{L} = 120 \mu\text{b}^{-1}$ due to the timescale, and thus contain approximately 46 thousand electron candidates after the selection. The E_T distributions at both collision energies exhibit the expected exponential decay shape and the flat η distribution except in the transition region. This behaviour is also expected (the simulation successfully mimics this behaviour) because of the degraded performance within this region. In Figure 5.1 the MC simulation events are normalized to the number of data events. As it can be seen, the data are roughly consistent with the MC simulation result. The slight deviation may be explained by the fact that the electron candidates in these data samples have peak transverse energy of about 4 GeV, which is significantly less than the optimal region of the electron identification algorithm designed for energies above 20 GeV. Also, as it will be revealed shortly, the majority of these candidate events are hadronic events, whereas the identification algorithm is designed for electrons.

An evaluation of the MC samples reveals that the electron candidates can be divided into two dominant components: electrons from photons converting in the detector material, and hadrons faking electrons. The former contribution corresponds to about 33% of all the electron candidates. Low energy hadrons may deposit most of their energies in the EM calorimeter, mimicking an electron signal and may be misclassified as electrons in the identification algorithm. In addition to the two dominant components mentioned,

there are also small contributions from semi-leptonic heavy quark decays (such as b and c quarks). However, they are expected to be less than 1% of all of the candidates.

5.1.2 Electron Identification Requirements

As mentioned above, less than half of the electron candidates identified by the standard ATLAS identification algorithm are real electrons and most of these do not come from primary collision vertex, but rather from interactions in the detector material. For some physics studies, it is beneficial to have a sample that consists of “pure” electrons, while other studies may require more statistics with looser quality requirements. In ATLAS, a series of additional selection requirements based on calorimeter and ID information are applied to each electron candidate, and categorized in three levels: loose, medium and tight. Each set of selection requirements has threshold values that are dependent on both E_T (divided into 11 bins) and on η (divided into 10 bins), but they are optimized for identification of electrons with transverse energies above 20 GeV. From previous studies using $Z \rightarrow e + e$ signal and QCD dijet MC samples with $E_T > 20$ GeV, the expected efficiencies are 94.3%, 90.0%, and 75.2% for loose, medium and tight selection, respectively [31]. For this part of the analysis, the same 46 thousand electron candidates from the early 7 TeV data are used, and thus contain very few electrons from primary interactions that are interesting for physics analysis. Correspondingly, the 7 TeV MC sample is chosen for comparison as described earlier. Due to the low energy of the electron candidates in the data samples, only the two lowest E_T bins in the electron identification selection requirements corresponding up to 10 GeV are used for this analysis.

An event sample passing tight selection criteria generally has higher purity and better

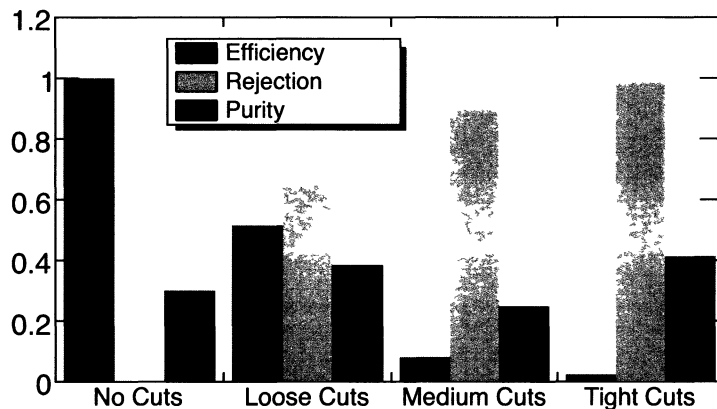


Figure 5.2: Evaluation of efficiency, rejection and purity for each category of electron identification algorithm. The results are from the 7 TeV MC simulation. In general, tighter cuts have higher rejection and purity, but lower efficiency as a consequence.

fake rejection, but lower efficiency as a consequence. This can easily be visualized in Figure 5.2. Efficiency, rejection and purity are calculated using MC simulation truth information, and they are:

$$\text{Efficiency} = \frac{\# \text{ real electrons selected}}{\# \text{ total real electrons}}, \quad (5.1)$$

$$\text{Rejection} = \frac{\# \text{ hadron fakes rejected}}{\# \text{ total hadron fakes}}, \quad (5.2)$$

$$\text{Purity} = \frac{\# \text{ real electrons selected}}{\# \text{ total events selected}}. \quad (5.3)$$

The loose electron selection uses exclusively the particle information from the calorimeter. In particular, EM shower width and shower containment variables from the second layer of the EM calorimeter, as well as ratio of energy leakage into the hadronic calorime-

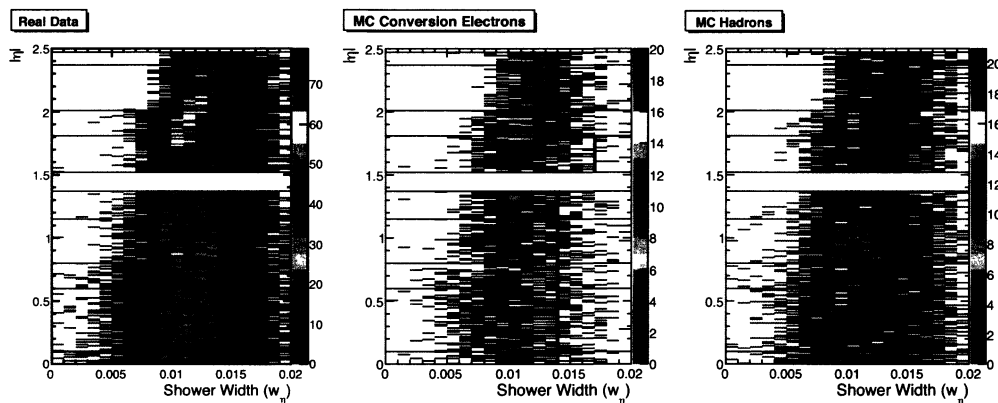


Figure 5.3: The shower width in η as a function of $|\eta|$. The black vertical lines indicate the cut values used for loose electron selection in the two lowest E_T bins (0 - 10 GeV). Events to the left of the cuts are accepted. Left: Real data / Centre: MC conversion / Right: MC hadrons.

ter to the total transverse energy deposited in the EM calorimeter cluster are used. As an example, the EM shower width in η is plotted in Figure 5.3. As it can be seen, the selection requirement on this variable removes the outliers in the tail region of the distribution, but fails to reject much of the hadron fakes.

The medium electron selection adds more selection criteria to the loose selection. In particular, it uses information from the first EM calorimeter layer such as the shower width in this layer. It also uses information from the ID for tracking quality, such as number of hits in pixel and SCT. As an example, the number of pixel layer hits is plotted in Figure 5.4. At first glance, the cut appears to reject most of the real electrons. However most of the electrons in the data sample are from photon conversions in the detector materials and these are being rejected by this requirement. These types of electrons are uninteresting for most physics analyses.

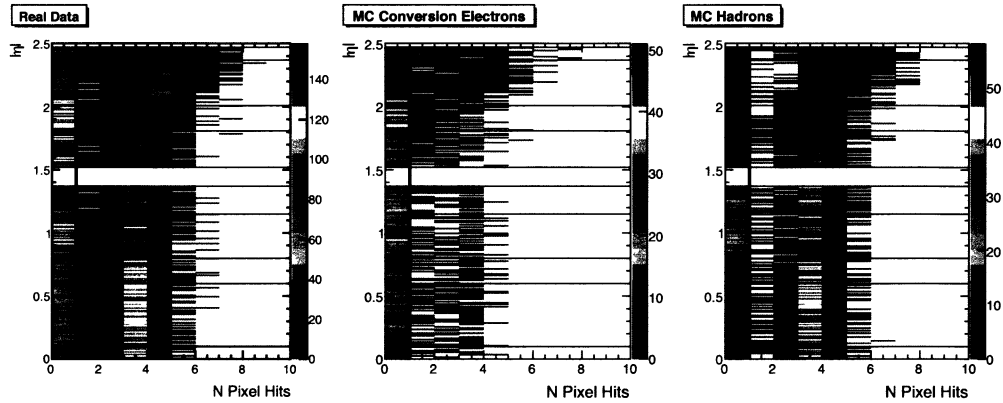


Figure 5.4: Number of hits in pixel detector as a function of $|\eta|$. The black vertical lines indicate the cut values used for medium electron selection in the two lowest E_T bins (0 - 10 GeV). Events to the right of the cuts are accepted. Left: Real data / Centre: MC conversion / Right: MC hadrons.

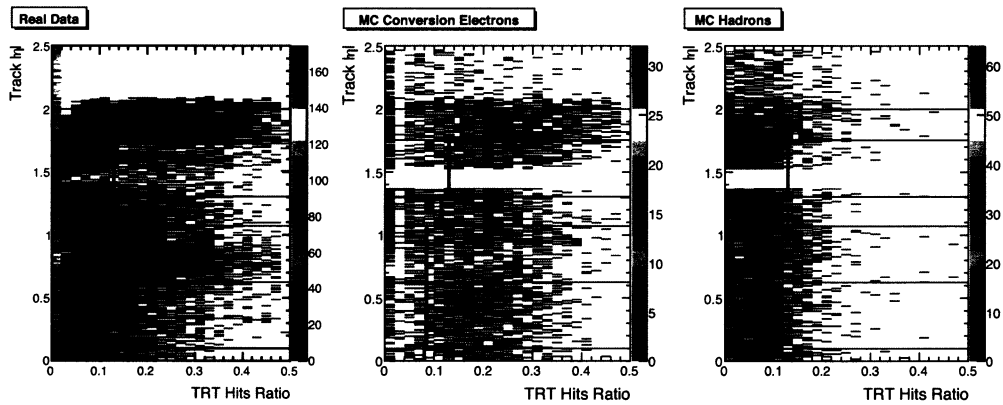


Figure 5.5: The ratio of high-threshold TRT hits to the total TRT hits as a function of $|\eta|$. The black vertical lines indicate the cut values used for tight electron selection in the two lowest E_T bins (0 - 10 GeV). Events to the right of the cuts are accepted. Left: Real data / Centre: MC conversion / Right: MC hadrons.

Finally, the tight electron selection is designed to exploit the full potential of the ATLAS detector to ensure that the particle is a non-conversion electron. In addition to the medium electron selection criteria, the tight selection requires further information from the ID, in particular from TRT and the b-layer (the first layer) of the pixel detector. The tight selection also makes use of combined calorimeter-ID information, for example the ratio of calorimeter energy to the track momentum. As an example, the ratio of high threshold TRT hits to the total TRT hits is plotted in Figure 5.5. Here the separation of the electron signal and the hadron fakes is obvious. Despite the increase in the purity at this stage, the efficiency suffers since all of the selection criteria, including loose and medium, are also applied at this stage (Refer to Figure 5.2).

The ATLAS electron selection requirements seem to separate and reject events that are expected to be rejected (such as electrons from photon conversions and hadrons faking electrons). However the data samples presented above mostly contain low energy electrons, and very few that come from primary collision vertex. The next section deals with the physical interaction process that produces electrons that come from primary collision with high E_T .

5.2 **W Boson Searches with Early Data**

In the Standard Model, the W and Z bosons are the force carriers of the weak force, responsible for nuclear decay as an example. They were first discovered at the Super Proton Synchrotron (SPS) at CERN in 1983 [33]. Their properties were studied in detail at the high energy e^-e^+ collider at the Large Electron-Positron collider (LEP) [34], and

Physics Process	Cross Section (nb)
$W \rightarrow e + \nu$	10.45
$W \rightarrow \tau + \nu \rightarrow e + \nu + \nu$	3.68
QCD Di-jet	1.15×10^6

Table 5.1: Cross section of each physics process considered for this analysis. The last two rows are the dominant backgrounds for the signal process. W cross sections are given at next-next-to-leading order and dijet cross sections are given at leading order [32].

the $p\bar{p}$ Tevatron collider at Fermilab has collected W and Z events for the past 20 years [7]. The high luminosity of the LHC will allow for more precise measurements of these gauge boson properties including mass measurements of the W boson, while the energy of the LHC allows these properties to be studied at a previously unexplored energy scale region.

Table 5.1 indicates the expected cross sections for each of the relevant processes to the W production at the centre-of-mass energy of 7 TeV, where the last two processes are the dominant backgrounds. Because of the relatively high cross-section of these interactions, searches for the W bosons are possible with early running of the LHC. The analysis detailed here is performed using events accumulated between April and May, 2010, with the integrated luminosity of $\mathcal{L} = 1.0 \text{ nb}^{-1}$.

5.2.1 Monte Carlo Samples and Expected Backgrounds

Three MC samples are used for this part of the analysis reflecting the three processes in Table 5.1. All of the MC simulations are generated using PYTHIA [25] and the full detector simulation was carried out using the GEANT4 simulation package [26]. The dataset names are as follows:

- **$W \rightarrow e + \nu$ (700 thousand events)**
(mc09_7TeV.106043.PythiaWenu_no_filter.recon.ESD.e468_s765_s767_r1253)
- **QCD filtered dijet (10 million events)**
(mc09_7TeV.105802.JF17_pythia_jet_filter.merge.AOD.
e505_e765_e767_r1305_r1306)
- **$W \rightarrow \tau + \nu \rightarrow e + \nu + \nu$ (100 thousand events)**
(mc09_7TeV.106022.PythiaWtaunu_1Lepton.merge.AOD.
e468_s765_s767_r1250_r1260)

The main background events for $W \rightarrow e + \nu$ events are non-electroweak processes, mostly from semi-leptonic decays of heavy quarks, electrons from photon conversion processes, and hadrons faking electrons. These backgrounds are generated as a filtered dijet sample, where the filter sums the transverse energies of all stable particles in a window of size $\Delta\eta \times \Delta\phi = 0.12 \times 0.12$ within $|\eta| < 2.7$ and only accepts events with summed $p_T > 17$ GeV.

In addition, $W \rightarrow \tau + \nu$ events contribute to the background, since the subsequent τ decay may create similar end-state signature as the signals ($W \rightarrow \tau + \nu \rightarrow e + \nu + \nu$).

5.2.2 W Identification

The leptonic decay channel $W \rightarrow \ell + \nu$ (ℓ is electron/muon and ν is neutrino) produces a typical signature inside ATLAS detector, where the signal events can be identified by searching for the lepton and missing energy representing an escaping neutrino in the same collision event. In order to identify these events, a series of selection cuts are applied in order to enhance the probability of detecting a high E_T electron, similar to the electron

candidate analysis in the previous section. This first set of requirements, referred to as “preselection”, is defined as follows:

- The collision event must be produced in a stable beam condition and under normal detector operational condition;
- The event must pass the level-1 trigger corresponding to an energy deposit of at least 2 GeV in the EM calorimeter;
- There must at least one particle identified as an electron by the lowest-level electron identification algorithm;
- Electron candidate transverse energy E_T must be greater than 20 GeV;
- Electron candidates must be in the η region dedicated to precision physics ($|\eta| < 2.47$), but not in the transition region ($1.37 < |\eta| < 1.52$);
- Electron candidates must not traverse known problematic areas of the calorimeter. Particles traversing these regions potentially lead to a mis-calculation of their properties. Such areas are identified, mapped and kept track of periodically.

On top of these preselection cuts, more stringent selections are applied to ensure that the event contains the W boson that decayed leptonically. Three additional selection criteria are defined which make up the so-called final selection requirements.

The first final selection requirement, designed to enhance the identification of high E_T electrons, requires that the electron candidate in the event satisfies a “tight” electron selection using information from both ID and the calorimeter as described in the previous section. By requiring the tight electron selection, the majority of electrons from photon conversion (i.e. not from the W boson decay) as well as hadrons faking electrons can be rejected.

The second final selection requirement, designed to identify events in which a neutrino may have been produced, requires the lower bound on the missing transverse energy E_T^{miss} of 25 GeV. E_T^{miss} is the inbalance in sum of energies in the transverse plane. The conservation of momentum requires that the net momentum as measured in the transverse plane must be zero. However, in the case where there exist particles in the same event that the detector is incapable of detecting, such as neutrinos, this results in an inbalance, or non-zero, sum of transverse energy. Because the leptonic W boson decay must have a neutrino, there must be non-zero E_T^{miss} . At the time of the analysis, the E_T^{miss} is reconstructed using calorimeter information only, and relies on a cell-based algorithm that assumes all interactions are purely electromagnetic, and ignores corrections due to difference in response due to hadronic activities or dead materials. The algorithm starts with a cell with energy deposit $E > 4\sigma_{noise}$, where σ_{noise} is the Gaussian width of the cell energy distribution in randomly triggered events. Then it iteratively gathers all neighbouring cells with energy deposit $E > 2\sigma_{noise}$. The final E_T^{miss} is calculated from (x,y) components from the cluster cells as follows:

$$E_T^{miss} = \sqrt{(E_x^{miss})^2 + (E_y^{miss})^2}, \quad (5.4)$$

where

$$E_{x,y}^{miss} = - \sum_{clusters} E_{x,y}. \quad (5.5)$$

The third final selection cut, designed specifically to identify W boson candidates, requires the lower bound on the transverse mass of lepton- E_T^{miss} system M_T of 40 GeV.

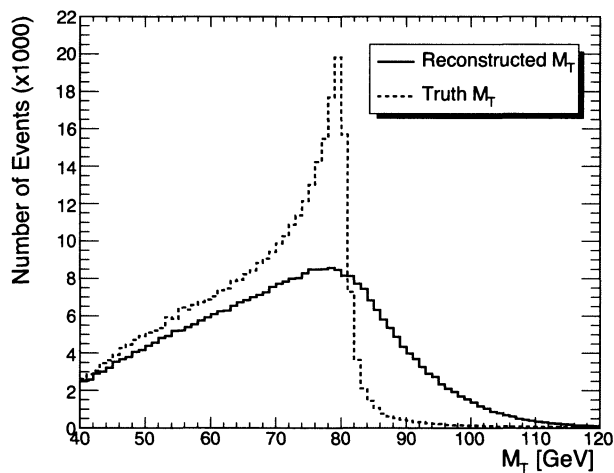


Figure 5.6: The spectrum of M_T from MC simulation. The number of events are in multiples of 1,000. The red dotted line uses truth simulation variables, whereas the black solid line is the fully simulated detector output.

M_T is defined as follows:

$$M_T = \sqrt{2E_T^\ell E_T^\nu \cdot \cos(1 - (\phi^\ell - \phi^\nu))}. \quad (5.6)$$

Because the detector cannot measure neutrino properties directly, it relies on E_T^{miss} information in (x, y) coordinates (see Equation 5.5). That is, $E_T^\nu = E_T^{miss}$ and the azimuthal angle of the neutrino ϕ^ν is calculated using (x, y) information from E_T^{miss} .

When the lepton and the E_T^{miss} correspond to electron and neutrino from the W boson decay, then the above equation describes the transverse mass of the W boson, and its distribution is depicted in Figure 5.6. As it can be seen, the true spectrum (red dotted line) has a Jacobian peak at ~ 80 GeV, and this corresponds to the mass of the

Requirement	Events after selection (Data $\sqrt{s} = 7 \text{ TeV}$)
Total for analysis	2.75×10^6
Triggered	2.73×10^6
Preselection	3456
Tight Electron	14
$E_T^{miss} > 25 \text{ GeV}$	6
$M_T > 40 \text{ GeV}$	6

Table 5.2: Number of candidate events after each selection requirement. After the final selection requirement, there are 6 candidate events.

W boson. Due to the degradation of detector resolution mainly from E_T^{miss} information, this peak is smeared and results in broader distribution (black solid line).

Table 5.2 summarizes the effect of each selection cut on the number of events. Preselection rejects most of the low quality events comprised of particles that are not triggered, low energy, failed to be identified as an electron by the identification algorithm, or traversing across bad regions of the detector or part of the detector not suitable for precision physics. Further rejection from the final selection requirements leads to the final selection count corresponding to $6_{-2}^{+3} W \rightarrow e + \nu$ candidates (error is calculated assuming Poisson statistics) for the integrated luminosity of $\mathcal{L} = 1.0 \text{ nb}^{-1}$.

5.2.3 *W* Properties in 7 TeV Data

As was demonstrated in Table 5.2, there are six $W \rightarrow e + \nu$ candidates out of 2.75 million collision events for the early ATLAS runs at $\sqrt{s} = 7 \text{ TeV}$. In this section, a comparison of the properties of data and the MC simulation is made. The MC samples used here are outlined in section 5.2.1 and consist of the $W \rightarrow e + \nu$ signal, and the

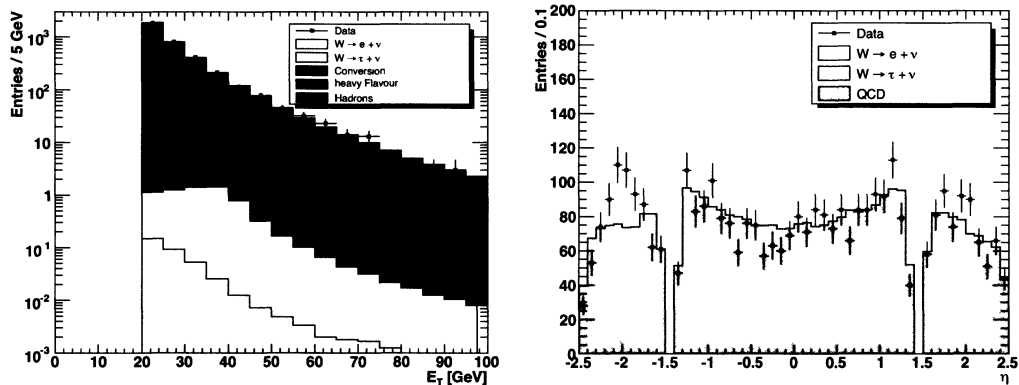


Figure 5.7: Kinematics properties of the events after preselection. Electron transverse energy E_T (left), and pseudorapidity η distribution (right).

dominant background, namely $W \rightarrow \tau + \nu$ and the QCD di-jets. All of the MC samples in this analysis are normalized to the number of events and to the integrated luminosity of $\mathcal{L} = 1.0 \text{ nb}^{-1}$ at the preselection level and final selection level, respectively.

Figure 5.7 shows the kinematics properties (E_T and η distribution) after preselection (MC normalized to number of data events). The different background contributions can be seen in the E_T distribution plot (note the logarithmic scale), with the $W \rightarrow e + \nu$ signal in white buried within the background. The η distribution plot (in linear scale) demonstrates that the events are predominantly from the QCD background. The discrepancy in the negative endcap region ($-2.5 < \eta < -1.5$) is due to poor-quality electron candidates that are rejected by application of the loose selection requirement.

Figure 5.8 shows the relationship between the E_T^{miss} and the M_T variables as defined in Equation 5.6 after applying the preselection and the tight electron requirement (MC normalized to $\mathcal{L} = 1.0 \text{ nb}^{-1}$). As it can be seen, there is a strong correlation between the

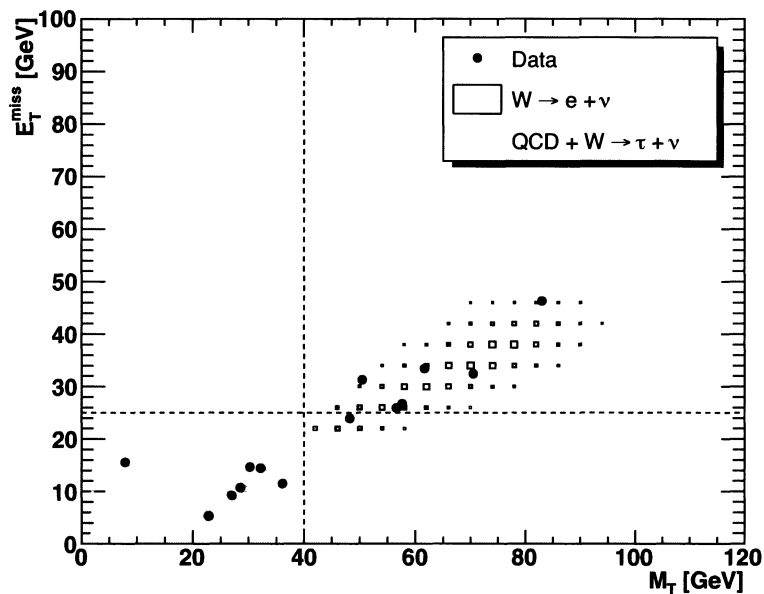


Figure 5.8: Two-dimensional plot showing the correlation of the missing transverse energy E_T^{miss} and the transverse mass of lepton- E_T^{miss} system

two variables. The dotted lines indicate the cut values for the two variables. It is evident that the cuts on the two variables effectively separate the signal (white squares) and the background (blue squares), with the background dominating the low E_T^{miss} and M_T space. In the plot, one can also see the six W candidates in the signal region indicated by the black points.

Figure 5.9 shows the effect of the E_T^{miss} cut on the M_T distribution. In other words, this is the projection of Figure 5.8 to the M_T axis on the bottom. The effect of E_T^{miss} is obvious, as it successfully rejects the background in the low M_T region. One can also see that after the E_T^{miss} cut, the W signal events become dominant. The six W candidates

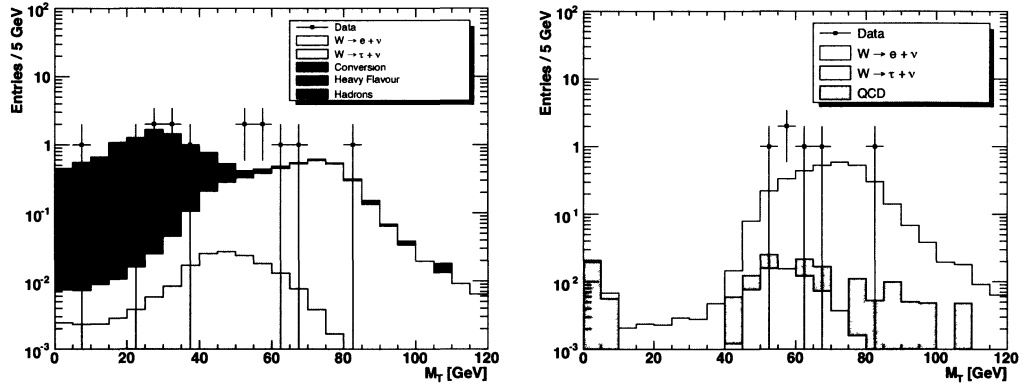


Figure 5.9: Distribution of the transverse mass of the lepton- E_T^{miss} system before (left) and after (right) the application of E_T^{miss} selection requirement.

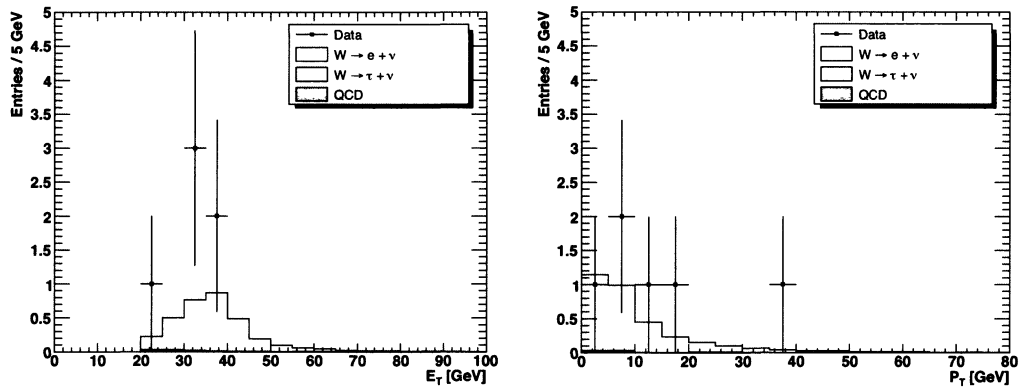


Figure 5.10: Left: E_T distribution of electrons after the final selection. Right: P_T distribution of the lepton- E_T^{miss} system after the final selection.

Events after selection (normalized to $\mathcal{L} = 1.0 \text{ nb}^{-1}$)			
Requirement	$W \rightarrow e + \nu$	$W \rightarrow \tau + \nu$	QCD dijets
Total for analysis	10.45	3.68	98990
Preselection	5.76	0.36	6734
Tight Electron	3.99	0.20	20
$E_T^{miss} > 25 \text{ GeV}$	3.25	0.09	0.23
$M_T > 40 \text{ GeV}$	3.24	0.08	0.18

Table 5.3: Expected number of signal and background events from MC simulation after each selection requirement.

can be seen again after the E_T^{miss} cut, in Figure 5.9 (right).

Figure 5.10 shows the E_T distribution of the electron candidates and the p_T of the lepton- E_T^{miss} system after the final selection (MC normalized to $\mathcal{L} = 1.0 \text{ nb}^{-1}$). Again, the signal dominates over the background after the final selection, and the six W candidates are visible in the figures.

Table 5.3 shows the expected number of signal and background events after application of the same selection requirements as outlined in Section 5.2.2. After the final selection, the expected number of signal events is 3.24 and 0.26 for the total background events (0.08 events from $W \rightarrow \tau + \nu$ and 0.18 from QCD dijet events).

5.3 Summary

Since the restart of the LHC, ATLAS has been accumulating proton-proton collision data. Preliminary analyses of these early ATLAS data at 900 GeV and 7 TeV centre-of-mass energies are presented. In particular, properties of electron candidates are presented in Section 5.1 and a first look at W boson candidates at 7 TeV collision energy is presented

in Section 5.2.

Six $W \rightarrow e + \nu$ candidates were produced at ATLAS in the first $\mathcal{L} = 1.0 \text{ nb}^{-1}$ of early collision runs. At this luminosity, 3.24 $W \rightarrow e + \nu$ signal events and 0.26 background events are expected from MC simulation. The results presented here are contained in the analysis at $\mathcal{L} = 6.7 \text{ nb}^{-1}$ presented at the PLHC (Physics at the LHC) conference in June 2010 [32]. At the integrated luminosity of $\mathcal{L} = 15 \text{ pb}^{-1}$ (corresponding to roughly 170 thousand W bosons), a MC simulation study shows that the precision of the W boson mass at the ATLAS experiment is expected to be $\delta_{m_W}/m_W \sim 0.15\%$ [14].

Chapter 6

Conclusion

Electrons are produced abundantly in collisions at the LHC, and the ATLAS detector is capable of identifying these electrons using its sophisticated inner detector and liquid-argon sampling calorimeter, both featuring new technology and design. The inner detector can withstand the high radiation flux of the LHC beams without compromising performance, while the liquid-argon calorimeter features the accordion geometry that allows uniform energy response in all directions. With these components, combined with proper calibration techniques, the identification of electrons is achieved with precise energy reconstruction (the linearity within $\sim 0.5\%$ for all energy scales). From the calibration analysis, it is found that the ATLAS EM calorimeter is very stable (no mean deviation from reference values over a 180-day study period) in terms of calibration constants used for energy reconstruction. The status of the solenoid has a small impact on delay and ramp by $\sim 0.1\%$ on their respective calibration constants.

Because of the complexity of the ATLAS detector, the energy measurement in the EM

calorimeter is sensitive to external factors. It is found that the simulation details used in electron energy response study alters the results slightly. Some of these are related to unintentionally-introduced errors, while others are intentionally inserted to mimic a realistic detector. The material distribution in the detector is found to have an impact on the energy response. From the simulation studies, it is found that the energy response is most sensitive to extra material in the inner detector, and primarily impacts beyond $|\eta| \sim 0.8$. In the context of W boson decays, it is found that bremsstrahlung of the boson has an impact on the energy reconstruction of the electron. The internal bremsstrahlung gives rise to the tail in the high response region, while external bremsstrahlung gives the tail in the low response region.

Since November 2009, ATLAS has acquired real collision data, and some electrons and W boson candidates have been identified. The electron candidates at $\sqrt{s} = 900$ GeV and $\sqrt{s} = 7$ TeV both agree with Monte Carlo simulation results. Because of the high population of low-energy events as a result of low luminosity ($9 \mu\text{b}^{-1}$ at $\sqrt{s} = 900$ GeV and $120 \mu\text{b}^{-1}$ at $\sqrt{s} = 7$ TeV), most of the electron candidates are either from photon conversions or hadrons faking electrons from QCD processes. The electron identification algorithm is not optimized for this category of events and thus purity and efficiency is low after application of tight selection requirement. A series of selection criteria has been defined and applied to collision data at $\sqrt{s} = 7$ TeV at an integrated luminosity of $\mathcal{L} = 1 \text{ nb}^{-1}$, and identified six $W \rightarrow e + \nu$ candidates. ATLAS continues to take collision data, and further analysis is in progress.

In conclusion, electron reconstruction and identification at the ATLAS experiment at the LHC has been discussed in detail, and the performance of the identification algorithm

has been studied both in simulation and in real collision data. Six $W \rightarrow e + \nu$ candidates are identified in this analysis, and their properties follow the expectations from the simulation results.

Appendix A

Personal Contributions to the ATLAS Collaboration

Within the duration of my two-year study period, I had a privilege to work as a member of the ATLAS collaboration and contributed my work. In this section, my personal contributions to the ATLAS collaboration are detailed.

1. Validation of liquid-argon EM calorimeter calibration constants
 - **Period:** May 2009 - September 2009
 - **Relevant Chapter:** Chapter 3
 - **Summary of contribution:** As a member of electronic calibration team, I was responsible for the validation of calibration constants of the LAr calorimeter in the calibration runs that were taken during the commissioning period. Studies of the stability of the calibration constants were also initiated. My contribution focused on the EM calorimeter in the barrel region. My contribution has been included as a part of [22], and also was mentioned in [35].
2. Liquid Argon System monitoring shifts

- **Period:** January 2010 - February 2010
- **Relevant Chapter:** N/A
- **Summary of contribution:** As a shifter, the responsibilities include monitoring of the LAr calorimeter status during the data taking (during this period they were cosmic-ray data), and reporting any deviation from the normal conditions. Other responsibilities include performing calibration runs whenever requested.

3. Contributions to the Egamma Working Group

- **Period:** May 2009 - April 2010
- **Relevant Chapter:** Chapter 4
- **Summary of contribution:** As a part of the Egamma (electrons and photons) working group, my research was focused on studying the various factors that impact the energy response of the calorimeter using Monte Carlo samples. The input from all of my contributions improved the electron calibration.

4. Identification of W bosons

- **Period:** April 2010 - June 2010
 - **Relevant Chapter:** Chapter 5
 - **Summary of contribution:** As a member of the WZ Observation Team, I was involved in the identification of W bosons in early collision data at $\sqrt{s} = 7$ TeV. My contributions include cross checks of W candidates after each selection requirement as detailed in Chapter 5, and evaluation of properties of these candidates. My contribution focused on the electron channel ($W \rightarrow e + \nu$). My contribution has been included as a part of [32] as well as [36]. I presented the preliminary result at the Canadian Association of Physicists (CAP) Congress that took place at the University of Toronto in June 2010 [37].
-

References

- [1] Peter W. Higgs. Broken symmetries, massless particles and gauge fields. *Phys. Lett.*, 12:132–133, 1964.
- [2] Claude Amsler et al. Review of particle physics. *Phys. Lett.*, B667:1, 2008.
- [3] The ALEPH, DELPHI, L3, OPAL, SLD Collaborations, the LEP Electroweak Working Group, the SLD Electroweak and Heavy Flavour Groups. Precision Electroweak Measurements on the Z Resonance. *Phys. Rept.*, 427:257, 2006, arXiv:hep-ex/0509008.
- [4] J. Boger et al. The Sudbury Neutrino Observatory. *Nucl. Instrum. Meth.*, A449:172–207, 2000, arXiv:nucl-ex/9910016.
- [5] Y. Fukuda et al. The Super-Kamiokande detector. *Nucl. Instrum. Meth.*, A501:418–462, 2003.
- [6] F. Abe et al. Observation of top quark production in $\bar{p}p$ collisions. *Phys. Rev. Lett.*, 74:2626–2631, 1995, arXiv:hep-ex/9503002.
- [7] John Ellison. W boson physics at the Fermilab Tevatron. *Acta Phys. Polon.*, B28:1271–1286, 1997, arXiv:hep-ex/9704001.
- [8] Lyndon Evans, (ed.) and Philip Bryant, (ed.). LHC Machine. *JINST*, 3:S08001, 2008.
- [9] G. Aad et al. The ATLAS Experiment at the CERN Large Hadron Collider. *JINST*, 3:S08003, 2008.

-
- [10] K. Aamodt et al. The ALICE experiment at the CERN LHC. *JINST*, 3:S08002, 2008.
- [11] R. Adolphi et al. The CMS experiment at the CERN LHC. *JINST*, 3:S08004, 2008.
- [12] A. Augusto Alves et al. The LHCb Detector at the LHC. *JINST*, 3:S08005, 2008.
- [13] John M. Campbell, J. W. Huston, and W. J. Stirling. Hard Interactions of Quarks and Gluons: A Primer for LHC Physics. *Rept. Prog. Phys.*, 70:89, 2007, arXiv:hep-ph/0611148.
- [14] G. Aad et al. Expected Performance of the ATLAS Experiment - Detector, Trigger and Physics. 2009, arXiv:0901.0512. CERN-OPEN-2008-020.
- [15] R. Fernow. *Introduction to experimental particle physics*. Cambridge University Press, Cambridge, 1986.
- [16] M. Delmastro. Electronic calibration of the ATLAS LAr calorimeters. Website: <http://indico.cern.ch/conferenceDisplay.py?confId=56168>.
- [17] Bernard Aubert et al. Performance of the ATLAS electromagnetic calorimeter end-cap module 0. *Nucl. Instrum. Meth.*, A500:178–201, 2003.
- [18] M. Aleksa et al. 2004 ATLAS Combined Testbeam: Computation and Validation of the Electronic Calibration Constants for the Electromagnetic Calorimeter. 2006. ATL-LARG-PUB-2006-003.
- [19] M. Delmastro. *Energy reconstruction and calibration algorithms for the ATLAS electromagnetic calorimeter*. PhD thesis, University of Milano, 2003.
- [20] D. Banfi et al. The measurement of the energy of electrons and photons in the ATLAS electromagnetic calorimeters. 2010. ATL-COM-PHYS-2010-068.
- [21] The LAr Electronic Calibration Team Twiki. Website: <https://twiki.cern.ch/twiki/bin/view/Atlas/LArCalibTeam>.
-

-
- [22] L. Courneyea et al. Computation and validation of the electronic calibration constants for the ATLAS Liquid Argon Calorimeters. 2010. ATLAS-COM-LARG-2010-008.
- [23] Electron Gamma Group Twiki. Website: <https://twiki.cern.ch/twiki/bin/view/AtlasProtected/ElectronGamma>.
- [24] G. Duckeck, (ed.) et al. ATLAS computing: Technical design report. 2005. CERN-LHCC-2005-022.
- [25] T. Sjostrand, S. Mrenna, and P. Skands. PYTHIA 6.4 physics and manual. *JHEP*, 5:026, 2006.
- [26] S. Agostinelli et al. GEANT4: A simulation toolkit. *Nucl. Instrum. Meth.*, A506:250–303, 2003.
- [27] D. Banfi. private communications, March 2010.
- [28] G. Unal. private communications, March 2010.
- [29] K. Whalen. Study of Extra Material in Front of the ATLAS Electromagnetic Barrel Calorimeter using High- p_T Electrons. Master’s thesis, Carleton University, 2009.
- [30] Distorted Material in CSC Simulation Twiki. Website: <https://twiki.cern.ch/twiki/bin/view/Atlas/DistortedMaterial>.
- [31] The ATLAS Collaboration. Electron and photon reconstruction and identification in ATLAS: expected performance at high energy and results at 900 GeV. 2010. ATLAS-CONF-2010-005.
- [32] The ATLAS Collaboration. Observation of $W \rightarrow \ell\nu$ and $Z \rightarrow \ell\ell$ production in proton-proton collisions at $\sqrt{s} = 7$ TeV with the ATLAS detector. 2010. ATLAS-CONF-2010-044.
- [33] G. Arnison et al. Experimental observation of lepton pairs of invariant mass around 95-GeV/ c^2 at the CERN SPS collider. *Phys. Lett.*, B126:398–410, 1983.
-

-
- [34] M. Thomson. Measurement of the mass of the W boson at LEP. *Eur. Phys. J.*, C33:s689–s693, 2004.
- [35] G Aad et al. Readiness of the ATLAS Liquid Argon Calorimeter for LHC Collisions. 2009, arXiv:0912.2642.
- [36] A. Ahmed et al. $W \rightarrow e\nu$ and $Z \rightarrow ee$ Observations supporting note. 2010. ATLCOM-PHYS-2010-297.
- [37] R. Ueno. Electron/Photon Candidates in Early ATLAS Data. Website: <https://indico.triumf.ca/contributionDisplay.py?contribId=166&sessionId=116&confId=953>.
-